

<https://doi.org/10.1038/s43247-024-01350-6>

# Decadal-to-centennial increases of volcanic aerosols from Iceland challenge the concept of a Medieval Quiet Period



Imogen Gabriel<sup>1</sup>✉, Gill Plunkett<sup>1</sup>, Peter M. Abbott<sup>1</sup>, Melanie Behrens<sup>1</sup>, Andrea Burke<sup>1</sup>,  
Nathan Chellman<sup>5</sup>, Eliza Cook<sup>1</sup>, Dominik Fleitmann<sup>1</sup>, Maria Hörhold<sup>3</sup>, William Hutchison<sup>1</sup>,  
Joseph R. McConnell<sup>1</sup>, Bergrún A. Óladóttir<sup>8</sup>, Johannes Preiser-Kapeller<sup>9</sup>, Jakub T. Sliwinski<sup>4,11</sup>,  
Patrick Sugden<sup>4</sup>, Birthe Twarloh<sup>3</sup> & Michael Sigl<sup>1,10</sup>

Existing global volcanic radiative aerosol forcing estimates portray the period 700 to 1000 as volcanically quiescent, void of major volcanic eruptions. However, this disagrees with proximal Icelandic geological records and regional Greenland ice-core records of sulfate. Here, we use cryptotephra analyses, high-resolution sulfur isotope analyses, and glaciochemical volcanic tracers on an array of Greenland ice cores to characterise volcanic activity and climatically important sulfuric aerosols across the period 700 to 1000. We identify a prolonged episode of volcanic sulfur dioxide emissions (751–940) dominated by Icelandic volcanism, that we term the Icelandic Active Period. This period commences with the Hrafnkatla episode (751–763), which coincided with strong winter cooling anomalies across Europe. This study reveals an important contribution of prolonged volcanic sulfate emissions to the pre-industrial atmospheric aerosol burden, currently not considered in existing forcing estimates, and highlights the need for further research to disentangle their associated climate feedbacks.

Volcanic aerosols are considered major drivers of natural climate variability, modifying the climate system through the reflection of incoming solar radiation, and subsequent cooling of the Earth's surface<sup>1,2</sup>. As a result, reconstructions of volcanic aerosol radiative forcing underpin climate model simulations, and the generation of accurate forcing estimates are therefore essential<sup>3,4</sup>.

The primary archives used for such reconstructions are the polar ice-core records. These highly resolved records provide insights into past volcanic activity over longer time periods (e.g., the last 11,500 years), through the preservation of sulfuric acid ( $H_2SO_4$ ) peaks. The synchronisation of these ice-core records on a global scale (Greenland and Antarctica), facilitates the generation of global volcanic radiative aerosol

forcing estimates (Fig. 1a<sup>5–7</sup>), which reveal periods of increased and reduced volcanic activity, for example, the Medieval Quiet Period<sup>8</sup>. The Medieval Quiet Period (700–1000 Common Era (CE)) was defined based on the scarcity of major tropical volcanic eruptions and minimal perturbations in solar forcing<sup>8</sup>. However, across this 300-year window, the Greenland ice-core records show an increase in background sulfate<sup>9</sup> (Fig. 1b). At the same time, proximal geological records of Icelandic volcanism, a source which has dominated the Greenland ice-core records through time<sup>6,10–13</sup>, suggest an increase in eruption frequency between 750 and 1000 CE<sup>14–18</sup> (Fig. 1c). Despite this, few volcanic eruptions have been detected within the Greenland ice-core records across the period<sup>19,20</sup> (Table 1).

<sup>1</sup>Climate and Environmental Physics & Oeschger Centre for Climate Change Research, University of Bern, 3012 Bern, Switzerland. <sup>2</sup>Archaeology & Palaeoecology, School of Natural and Built Environment, Queen's University Belfast, Belfast BT7 1NN, UK. <sup>3</sup>Alfred-Wegener-Institut Helmholtz-Zentrum für Polar- und Meeresforschung, 27570 Bremerhaven, Germany. <sup>4</sup>School of Earth and Environmental Sciences, University of St Andrews, St Andrews KY16 9TS, UK. <sup>5</sup>Desert Research Institute, Nevada System of Higher Education, Reno, NV 89512, USA. <sup>6</sup>Physics of Ice, Climate and Earth, Niels Bohr Institute, University of Copenhagen, 2200 Copenhagen, Denmark. <sup>7</sup>Department of Environmental Sciences, University of Basel, 4056 Basel, Switzerland. <sup>8</sup>Icelandic Meteorological Office, 105 Reykjavík, Iceland. <sup>9</sup>Department of Byzantine Research/Institute for Medieval Research, Austrian Academy of Sciences, A-1010 Vienna, Austria. <sup>10</sup>Department of Geosciences, University of Oslo, 0371 Oslo, Norway. <sup>11</sup>Present address: School of Oceanography, University of Washington, Seattle, WA 98195-7940, USA. e-mail: [imogen.gabriel@unibe.ch](mailto:imogen.gabriel@unibe.ch)

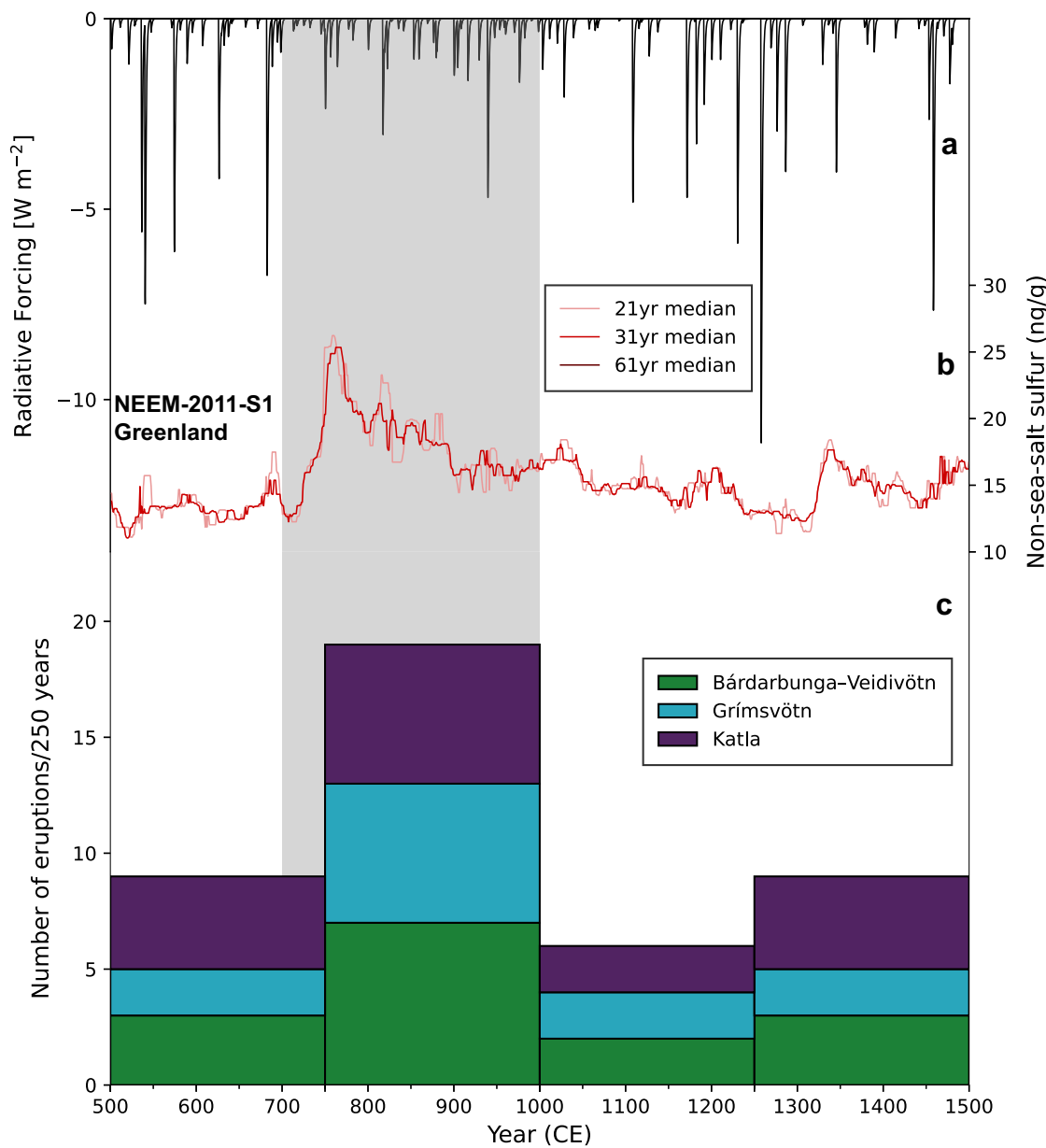


**Fig. 1 | Global, Regional, and Proximal records of volcanic activity between 500 and 1500 CE.** **a**, Radiative forcing<sup>5,7</sup> between 500 and 1500 CE. A reduction in forcing can be observed between 700 and 1000 CE; **b**, 21-year, 31-year, and 61-year median non-sea-salt Sulfur (nss-S) concentrations for NEEM-2011-S1. Concentrations are elevated compared to the periods before and after; **c**, estimated eruptive frequency of

Katla, Grímsvötn and Bárðarbunga-Veiðivötn volcanic systems in 250-year time windows, determined using the Catalog of Icelandic Volcanoes<sup>154</sup> and published literature<sup>16,32,155–158</sup>. An increase in eruptive frequency from all volcanic systems is observed during the period 751–1000 CE. The Medieval Quiet Period (700–1000 CE) is indicated by the gray shading.

Existing volcanic detection methods, which facilitate the distinction between the non-volcanic (i.e., marine, biogenic, anthropogenic) and volcanic sulfate deposited within the ice, as sulfur has a number of different sources<sup>21</sup>, use the implicit assumption that volcanic sulfate depositional signals are sharp and short-lived (up to 3 years), due to the short atmospheric lifetime of sulfate<sup>10</sup>. However, geological records show that this assumption may not hold true, with evidence of eruptions lasting for several decades to centuries<sup>22,23</sup>, including eruptions from Iceland<sup>6,18,24,25</sup>. Due to the proximity of Greenland to Iceland, such long-lasting eruptions may be imprinted in the ice-core sulfate records, resulting in long-term changes which introduce ambiguity for secure detection and quantification of volcanic contributions. At present, clear diagnostic tracers unique to volcanic eruptions are missing within the polar ice which would facilitate in both their detection and source attribution and thus allow the distinction between both short-lived eruptions and longer lasting volcanic episodes.

Here, we present a set of four distinct diagnostic tracers (cryptotephra, sulfur isotopes, halogens, and heavy metals) within the ice-core records, which when combined, can characterize important source parameters i.e., exact location and plume height of past eruptions. We apply this multi-proxy toolkit across the time period 700–1000 CE, resolving existing mismatches between proximal Icelandic records and global volcanic radiative aerosol forcing estimates through the attribution of these events within the Greenland ice cores. Finally, we explore the climate impacts at the onset of this period of elevated background sulfate, using proxies and documentary evidence.

## Results

The seven Greenland ice cores (NEEM-2011-S1, NGRIP1, NGRIP2, EGRIP, RECAP, B19, and TUNU2013) used within this study are located across the Greenland ice sheet (see Fig. 2, Supplementary Table 1) between

**Table 1 | Correlated volcanic eruptions within Greenland ice-core records 700–1000 CE**

Eruption Age (Year CE) [Name if applicable]	Volcanic system <sup>a</sup>	Eruption Style	Minimum estimated eruptive volume (km <sup>3</sup> )	Estimated Volcanic Stratospheric Sulfur Injection (VSSI Tg S) <sup>b</sup>	Refs.
753 <sup>c</sup>	Grímsvötn, Iceland (B)	Explosive	NA	6.79	This study
757 <sup>c</sup>	Katla, Iceland (B)	Explosive	NA	3.07	This study
763 ± 1 <sup>c</sup> [Hrafnkattal]	Katla, Iceland (B)	Explosive	4.5	4.77	15 <sup>c</sup> ; This study
781 ± 2 <sup>c</sup>	Grímsvötn, Iceland (B)	Explosive	NA	1.72	16 <sup>c</sup> ; This study
822 [K-822]	Katla, Iceland (B)	Explosive	0.4	3.93	15,33,105
853 [WRAe/AD860B]	Mt Churchill; USA (R)	Explosive, Plinian	39.4	2.48	20,103,150
877 <sup>c</sup> [Settlement Layer]	Torfajökull and Bárðarbunga-Veidivötn, Iceland (R + B)	Plinian, Phreatomagmatic	5	3.05	15 <sup>c</sup> ; This study
940 [Eldgjá]	Katla, Iceland (B)	Effusive, Strombolian, Phreatomagmatic	1.3	16.23	15 <sup>c,2</sup>
946 [Millennium eruption]	Changbaishan, China/DPRK (T/RD)	Explosive, Plinian	40	1.72	20,103,153

Eruption Age (Year CE) and common name (if applicable), correlated volcanic system, eruption style, minimum estimated eruptive volume (km<sup>3</sup>), estimated Volcanic Stratospheric Sulfur Injection (VSSI Tg S) are provided.

<sup>a</sup>No existing eruptive volume estimate available.

<sup>b</sup>Where magmatic composition is indicated by (B) Basaltic, (R) Rhyolitic, (T) Trachytic, and (RD) Rhyodacitic.

<sup>c</sup>Summary of identified volcanic eruptions within the Greenland ice-core records, including previous attributions and those made within this study.

elevations of 2100 m above sea level (a.s.l) and 3000 m a.s.l. These ice cores are all dated by annual-layer counting (NEEM-2011-S1, NGRIP1, EGRIP, RECAP, B19, and TUNU2013 records are all volcanically synchronised to the NS1-2011 chronology<sup>26</sup>, whilst the NGRIP2 record uses the DRI\_NGRIP2 chronology<sup>27</sup>). Together, they fully cover the period 700–1000 CE, with a dating uncertainty during this 300-year period better than ±2 years, constrained by two calendar dated cosmogenic age markers in 774 CE and 993 CE (see Methods, Supplementary Table 2). For consistency, we will use the mean of these two age models which may differ by ±1 year as will be shown later in individual figures. Details on the analytical methods employed for each ice core are provided (Methods, Supplementary Table 1).

We present stacked annual non-sea-salt (nss) sulfur concentrations ( $N=6$ ), which show an abrupt increase in 751 CE; prior to this, sulfur concentrations were lower overall, with less frequent variability (Fig. 3a). Median sulfur concentrations between 751 and 940 CE (the latter date marking the Eldgjá fissure eruption from the Katla volcano<sup>28</sup>) were elevated by a factor of 1.6 compared to the period 700–750 CE (Fig. 3a). Superimposed on these increased background values are frequent sulfate peaks lasting between 1–12 years, with a sulfur concentration increase in 751–763 CE marking this transition.

Stacked nss chlorine ( $N=6$ ), fluorine ( $N=2$ ), and non-crustal (nc) bismuth and thallium ( $N=4$ ) concentration records strongly resemble the overall structure of the nss sulfur record, but with a more pronounced step-change at 751 CE (Fig. 3b, c). Throughout the 751–763 CE episode, element concentrations are elevated (8-fold increase for F, 4-fold increase for Cl, 12-fold increase for Tl, and 5-fold increase for Bi) and remain elevated above pre-event levels for ~12 years. Though concentrations decrease again after 765 CE, the overall concentrations remain elevated (3-fold increase for F and 2-fold increase for Cl, Tl, and Bi) and highly variable in contrast to the first half of the 8th century, where concentrations of nss chlorine (2.9 ng/g), fluorine (0.2 ng/g) and the heavy metals thallium (0.04 pg/g) and bismuth (0.06 pg/g) are low. Correlations between volatile metals (Tl, Bi) and volcanic volatiles (Cl, S) are strong throughout the period 751–940 CE, particularly for the 751–763 CE episode, suggesting a common source, transport, and deposition of these species. This is in agreement with ref. 29 who used Tl to assess past volcanic emissions of heavy metals (Bi, lead, cadmium) in Antarctic ice during the Common Era and ref. 30 who propose that volatile metals from volcanic sources can be transported to nearby ice-core sites (i.e., 400 km distance) as water soluble aerosols, forming metal-halogen complexes.

To constrain the source of the volcanic events we searched for cryptotephra in the B19, TUNU2013, and RECAP ice cores. Guided by exactly co-registered analyses of size resolved insoluble particle concentrations and sulfur (see Fig. 3a, Supplementary Fig. 1), we successfully identified cryptotephra in the following years: 753 CE, 757 CE, 763 CE, 766 CE, 781 CE, 877 CE in B19 and TUNU2013. Notably, ice samples with cross sectional areas of up to 15 cm<sup>2</sup> and correlated to the years 763 CE and 877 CE, had high abundances of volcanic glass shards (up to 4000). Through geochemical analyses (see Methods), correlations were made with the Katla, Grímsvötn, Bárðarbunga-Veidivötn, and Torfajökull Icelandic volcanic systems, as outlined below, with sample identification based on ice-core site, depth, and estimated age. A detailed description of shard characteristics and concentrations can be found in the Supplementary Data.

Major (see Fig. 4 and Supplementary Fig. 2) and trace element (see Supplementary Fig. 3) analysis of individual glass shards from six samples obtained from the three ice cores between 751 and 763 CE can be correlated to the Grímsvötn (B19\_149.88m\_753CE) and Katla (B19\_149.60m\_757CE; B19\_148.88m\_763CE; TUNU2013\_158.20m\_762CE) volcanic systems. The 753 CE glass shards were yellowish-green in color with thin-platy morphologies (see Supplementary Fig. 4a), whilst the 757 CE and 763 ± 1 CE glass shards (up to 50 µm in size within all ice samples) were yellowish-brown in color, with platy morphologies, and a TiO<sub>2</sub>-rich basaltic composition characteristic of the Katla volcanic system (see Supplementary Fig. 4b–f). We geochemically correlated the 763 CE ice-core tephra

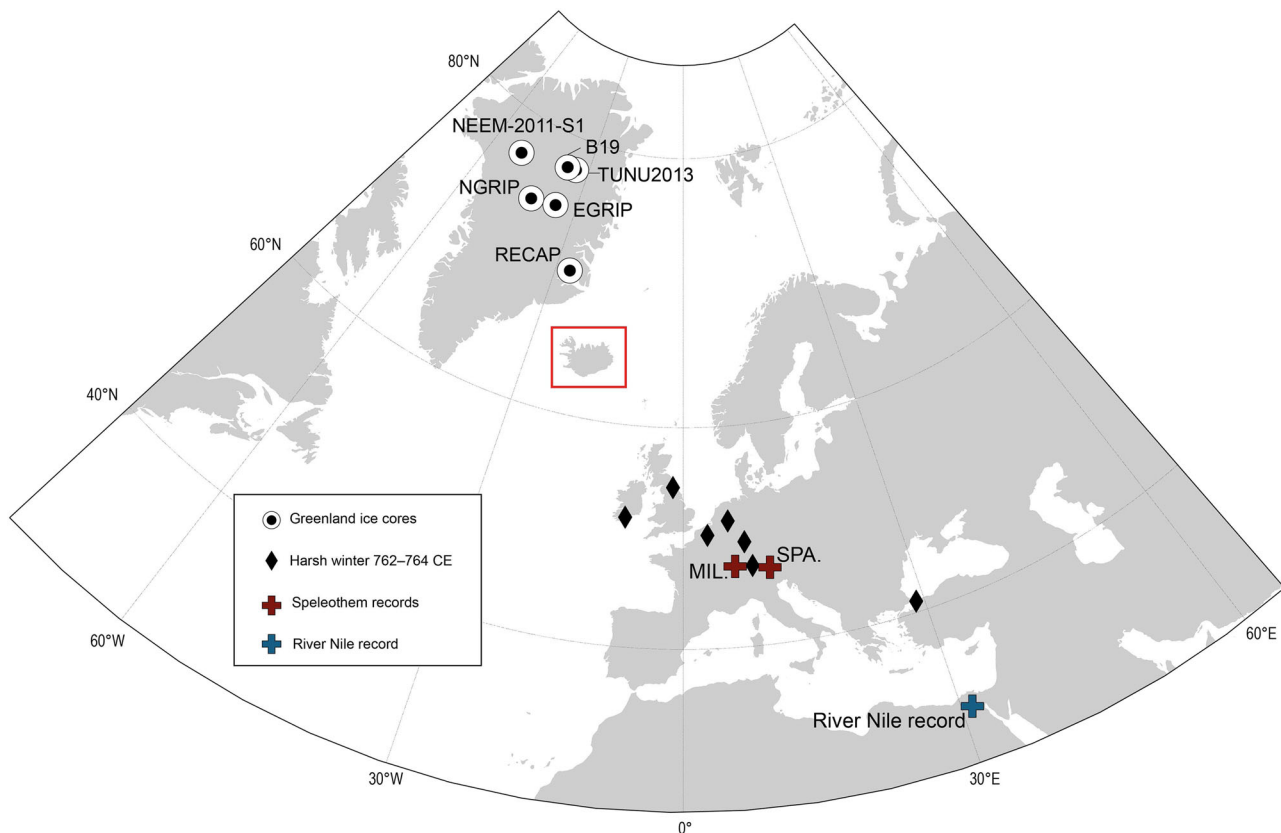


**Fig. 2 | Cooling anomalies in the North Atlantic region.** Map showing the location of the Greenland ice core sites (B19, TUNU2013, NEEM-2011-S1, NGRIP, EGRIP, and RECAP) used within this study. The locations of the Milandre (MIL) and Spannagel (SPA) speleothem records (red crosses) and River Nile low stand record (blue cross) utilised within this study are indicated. The black diamonds denote

harsh winters in the years following the  $763 \pm 1$  CE Hrafnkatla volcanic eruption across Europe, as cited in the historical written records<sup>68</sup>. The red rectangle highlights the location of the correlated volcanic systems within this study, with a detailed map found in Supplementary Fig. 10.

(B19\_148.88m\_763CE and TUNU2013\_158.20m\_762CE, RECAP\_297.44m\_762CE) with proximal material from the Icelandic Hrafnkatla eruption, including glass from identified tephra horizons in soil sections  $\sim 20$  km from the main Katla vent (see Methods). The Hrafnkatla eruption<sup>14,16,31</sup>, also referred to as AT-8 or E2 within the literature<sup>15,32</sup>, was a major tephra-producing eruption from the Katla volcanic system, with an estimated total bulk volume of  $>4.5$  km<sup>3</sup><sup>15</sup>. This is the earliest tephra-producing Katla volcanic eruption during the Common Era to be geochemically identified within the Greenland ice-core records and marks the end of a  $\sim 12$ -year period of continuous volcanic activity from Icelandic volcanic systems which here we term the Hrafnkatla episode.

Limited geochemical analyses were obtained for the  $766 \pm 1$  CE sample (B19\_148.67m\_766CE) and therefore, a definitive source could not be identified. However, due to the abundance of other material observed in the sample, including minerals and black particles of a similar size to the tephra shards, it is possible that the glass shards were deposited at the site with these other particles via the same secondary processes<sup>33</sup>. Additional geochemical analyses of this sample (on both the tephra glass and other particles) could help test this hypothesis.

Analysis of the  $781 \pm 2$  CE sample (B19\_147.29m\_781CE) provided a correlation to a Grímsvötn tephra identified in Lake Lögurinn, Iceland<sup>16</sup> (see Fig. 4 and Supplementary Fig. 5). The B19\_147.29m\_781CE glass shards (up to 50  $\mu\text{m}$  in size within all ice samples) were greenish in color, with platy morphologies (see Supplementary Fig. 4g). Within the lake, this horizon has been dated to 788 CE using the lake chronology (constructed using radio-carbon dating and historical tephra). This horizon is thus considered to be the most likely correlative for B19\_147.29m\_781CE as it is the only Grímsvötn event reported in the proximal records within  $\pm 50$  years.

A correlation was also made between the 877 CE event in the B19 ice core to the Settlement Layer ( $877 \pm 2$  CE) in Iceland using proximal material which was analyzed simultaneously (see Fig. 4 and Supplementary Fig. 6). Both the silicic and basaltic components of the event, attributed to the Torfajökull and Bárðarbunga-Veiðivötn systems respectively, were identified in the B19 ice core, with glass shards having clear, greenish platy morphologies (see Supplementary Fig. 4h). The Settlement Layer is widely dispersed across Iceland and is considered an important horizon for separating the pre-historic (i.e., before 877 CE) and historic (i.e., after 877 CE) periods, defining the approximate date of the Viking settlement of Iceland<sup>34</sup>. The silicic and basaltic components of this horizon have previously been identified in the GRIP, GISP2, and TUNU2013 ice cores<sup>19,35,36</sup>, providing an important tie-point for the synchronisation of records.

The multiple correlations made within the Greenland ice-core records to Icelandic volcanic systems during the 751–940 CE period align well with reconstructions of volcanic activity from proximal Icelandic geological records. Proximal geological records show an increase in activity (i.e., eruption frequency and cumulative tephra volume) of the Katla and Bárðarbunga-Veiðivötn systems during the period 751–940 CE compared to earlier and later time-periods<sup>14,15</sup> (see Fig. 1c). Centennial mean tephra volume (minimum volume dense rock equivalent (DRE)) from Katla volcanic eruptions was 0.1 km<sup>3</sup> between 1–750 CE, increasing to 2.0 km<sup>3</sup> between 751–940 CE and decreasing to 0.1 km<sup>3</sup> between 941–1755 CE<sup>15</sup>. This fluctuation has been linked by volcanologists to the presence of a relatively shallow magma chamber that was active prior to the 939 CE Eldgjá eruption<sup>15</sup>. Owing to the strong agreement between the two records which suggest Icelandic volcanic systems were highly active and productive over

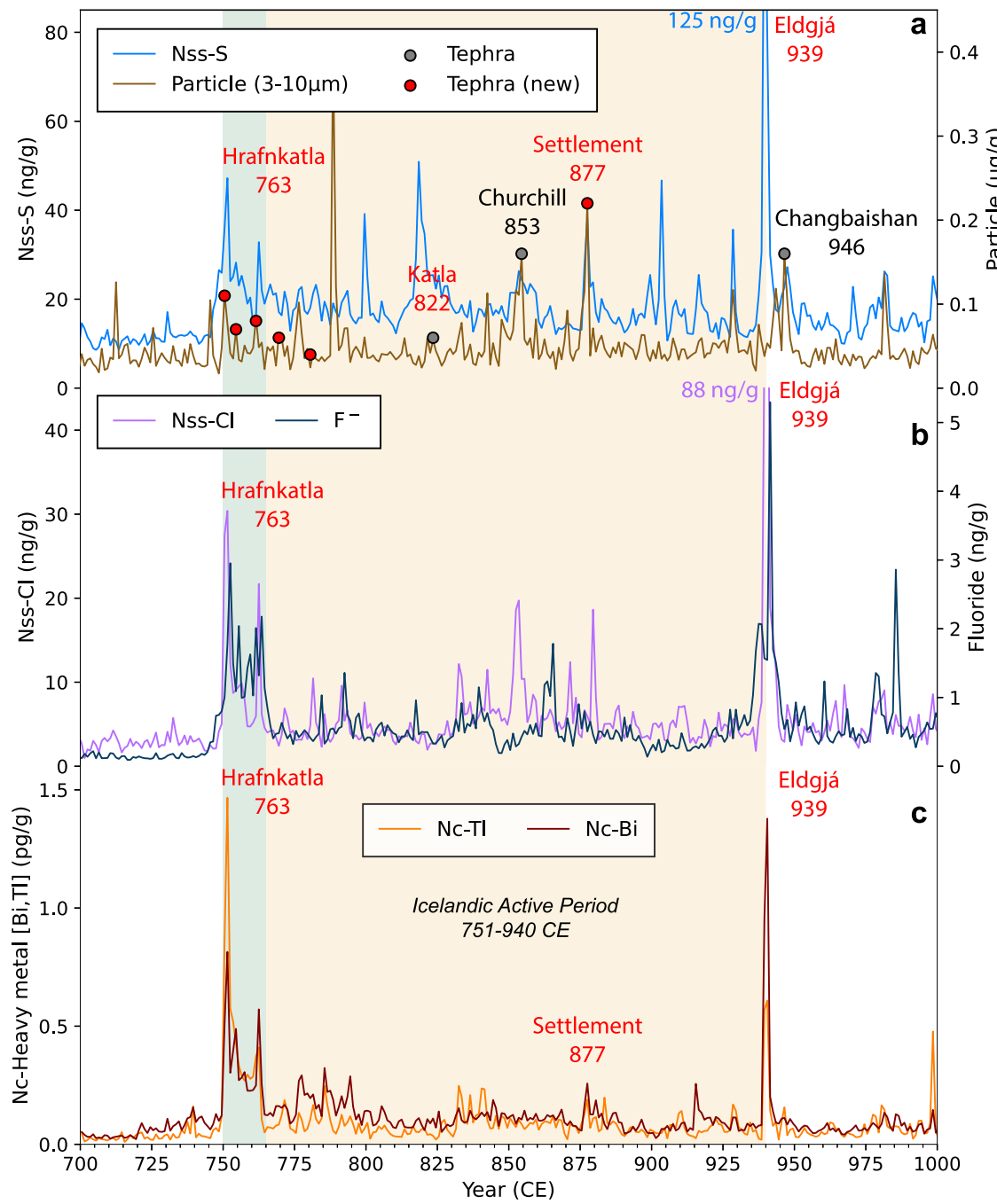


**Fig. 3 | Greenland ice core volcanic tracers across 700–1000 CE.** **a** Non-sea-salt Sulfur (nss-S) stack ( $N = 6$ ) of Greenland ice cores and associated insoluble particle record (3–10  $\mu\text{m}$ ). The locations of existing sampled tephra (gray) across this time period are denoted, where correlations have been made to the 822 CE eruption of Katla, Iceland<sup>33</sup>, 853 CE eruption of Mt Churchill, USA<sup>20,100</sup>, and 946 CE Changbaishan, China/DPRK<sup>20,103</sup>. New samples which form part of this study are shown by the red circles; **b** Non-sea-salt chlorine (Nss-Cl) stack ( $N = 6$ ) and Fluoride (F<sup>-</sup>) stack ( $N = 2$ ) of Greenland ice cores; **c** Non-crustal thallium (Nc-Tl), non-crustal bismuth (Nc-Bi) stack ( $N = 4$ ) of Greenland ice cores. The blue shading denotes the Hrafnkatla episode (751–763 CE), and the beige shading shows the duration of the Icelandic Active Period (751–940 CE).

the period 751–940 CE, we subsequently term this period the Icelandic Active Period (IAP).

To further investigate this abrupt shift in background sulfate, and thus the onset of the IAP which commenced with the Hrafnkatla episode (751–763 CE), we measured S isotopes in sulfates at high-temporal resolution across this 12-year period on the TUNU2013 ice core (see full details in Methods). Mean  $\delta^{34}\text{S}$  values (see Methods for details) across the Hrafnkatla episode are +6.4‰ (see Fig. 5b). These values are lower compared to previously measured mean  $\delta^{34}\text{S}$  TUNU2013 background samples ( $+9.5\text{‰} \pm 0.9\text{‰}$ )<sup>37</sup>, and thus suggest a largely volcanic origin. Background

sulfate consists of both marine and volcanic emissions, and an increase in volcanic sulfate results in lower  $\delta^{34}\text{S}$  values within the ice (i.e., values closer to 0‰), as observed across the Hrafnkatla episode. Background corrected  $\delta^{34}\text{S}$  values over this period are +2.6‰ ( $\pm 2.5\text{‰}$ ) (see Supplementary Fig. 7). The anti-correlation between the local S peaks and the  $\delta^{34}\text{S}$  further suggests large contributions of sulfur with a volcanic origin. Cryptotephra was identified in samples with low (at or below −0.6‰)  $\delta^{34}\text{S}$  values (see Fig. 5a).

Previous polar ice-core studies<sup>37–42</sup> have successfully utilised  $\Delta^{33}\text{S}$  (see Methods for details) isotopic values to determine whether sulfate aerosol formation occurred in the stratosphere, or more precisely above the ozone

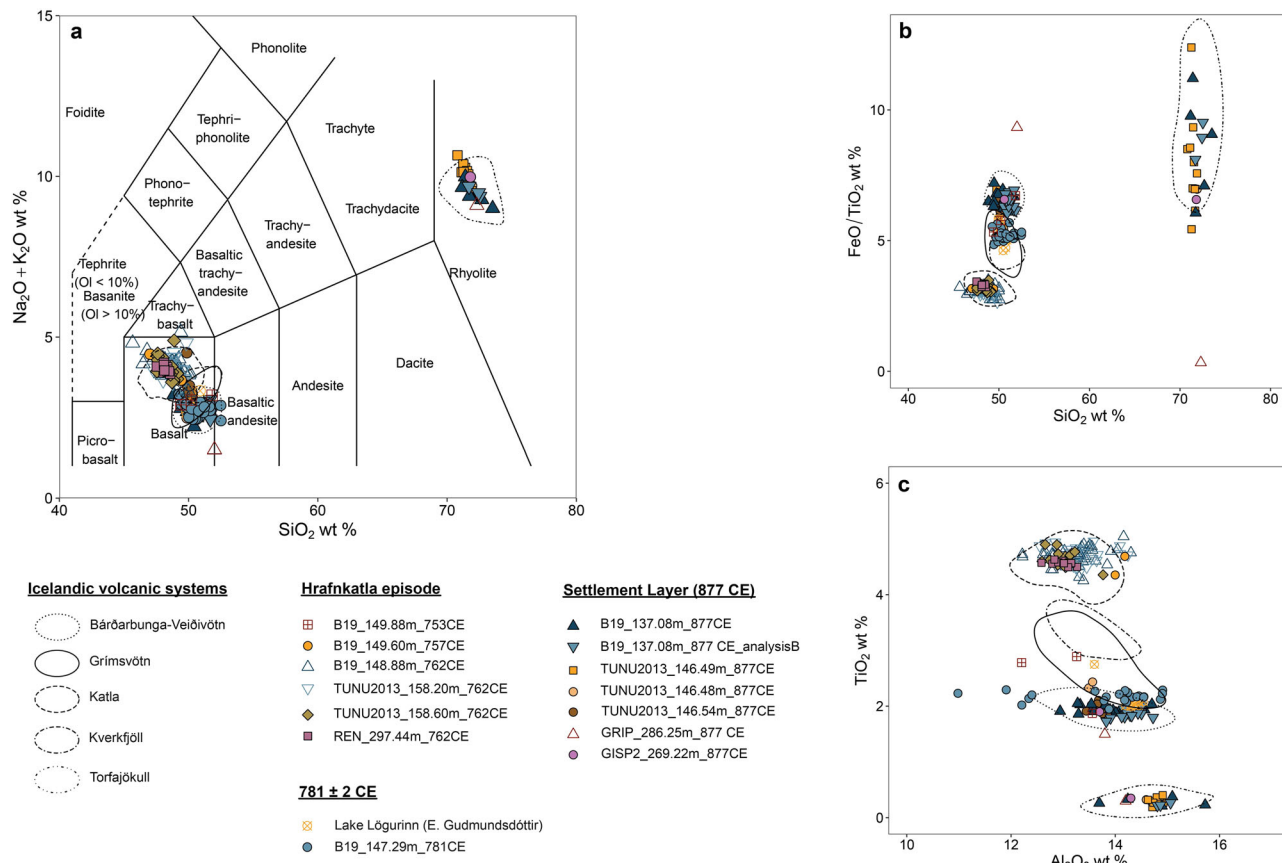


**Fig. 4 | Pinpointing the source volcanoes of the Icelandic Active Period.** Major element geochemical glass shard analyses from cryptotephra samples from the B19, TUNU2013, and RECAP ice core across the Icelandic Active Period. Samples have been grouped by event (Hrafnkatala episode,  $781 \pm 2$  CE, and Settlement Layer), as indicated by the legend. All data have been plotted based on (a) magmatic composition- Total Alkali ( $\text{Na}_2\text{O} + \text{K}_2\text{O}$ ) vs Silica ( $\text{SiO}_2$ )<sup>159</sup>, and major element bi-plots of (b)  $\text{FeO}/\text{TiO}_2$  vs  $\text{SiO}_2$  and (c)  $\text{TiO}_2$  vs  $\text{Al}_2\text{O}_3$ . Geochemical fields for the Grímsvötn,

Katla, Bárðarbunga-Veiðivötn, Þorðajökull, and Kverkfjöll Icelandic volcanic systems have been constructed based on published data<sup>(14,160–173)</sup>. For the Settlement Layer event, published ice core analyses from GRIP<sup>35</sup>, GISP2<sup>36</sup>, and TUNU2013<sup>19</sup> are shown for reference. All data have been normalized to 100 % (anhydrous basis). Individual geochemical plots for the Hrafnkatala episode,  $781 \pm 2$  CE, and Settlement Layer events can be found in Supplementary Figs. 2, 5, 6 respectively.

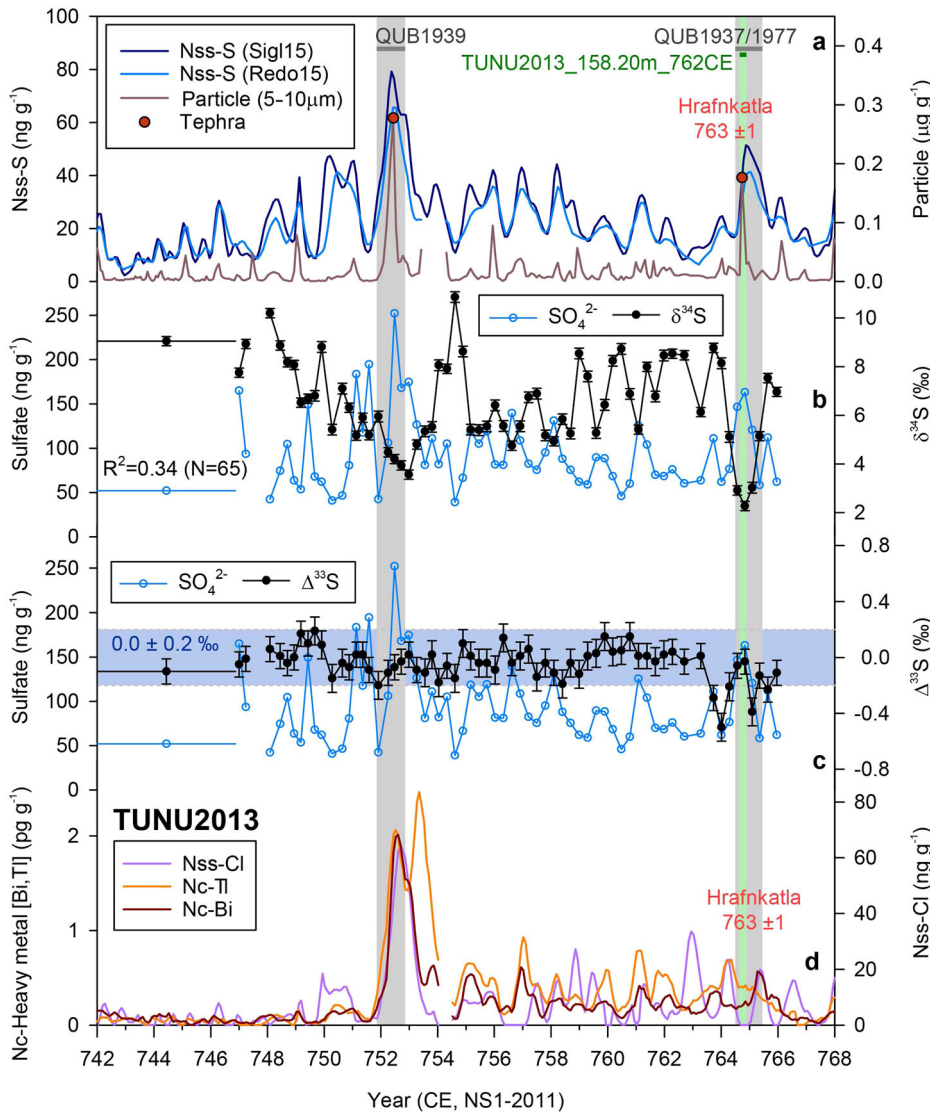
layer, which above Iceland is located between 11 and 15 km<sup>43</sup>, thus providing an indication of relative plume height. Our analysis of  $\Delta^{33}\text{S}$  across the Hrafnkatala episode has revealed that this volcanic sulfate mainly has values varying between  $-0.2$  and  $+0.2\text{‰}$  for  $\sim 12$  years (see Fig. 5c). These values are indistinguishable from the 2. s.d. of a non-mass-independent-fractionation secondary standard (see Methods) and indicate a  $\sim 0\text{‰}$   $\Delta^{33}\text{S}$  value, and hence a dominant tropospheric origin for the S fallout. However, in 762/3 CE, values fall to  $-0.5\text{‰}$ , suggesting that this prolonged elevated tropospheric phase culminated in a short-lived stratospheric phase, which through cryptotephra geochemical analysis we have correlated to the Katla Hrafnkatala volcanic eruption (see Fig. 5a). This is the first detection within the ice-core records, to the best of our knowledge, of anomalous  $\Delta^{33}\text{S}$  values for an Icelandic eruption, and unlike tropical stratospheric eruptions (i.e., Samalas 1257 CE and Tambora 1815 CE<sup>37</sup>), the  $\Delta^{33}\text{S}$  anomaly is much smaller for this high-latitude stratospheric Icelandic eruption. This difference can be attributed to the simultaneous deposition of tropospheric and stratospheric S, resulting in a muted anomalous  $\Delta^{33}\text{S}$  value<sup>44</sup>.

No sulfur isotope analyses have been performed for the remaining part of the IAP, but sulfur concentrations in the Greenland ice cores frequently exceed typical levels which were prevalent for the first half of the 20th century during periods of intensive industrial activity and related sulfur emissions across the North Atlantic region<sup>45</sup> (Fig. 6a). Considering the high activity of these Icelandic volcanic systems across the study period, as revealed through the application of the above proxies, traditional approaches to isolate and quantify volcanic eruptions and

their sulfur emissions are inevitably biased. This has resulted in an underestimation in the number, total duration, and  $\text{SO}_2$  emission strength of volcanic events. For example, both the reconstructions of ref. 46, the recommended volcanic forcing for the Paleoclimate modeling intercomparison project (PMIP) 3 model experiments, and ref. 47, did not detect any volcanic events between 751 and 763 CE (see Supplementary Fig. 8). This is because existing reconstructions of volcanic sulfate deposition used in these forcing estimates (e.g., NGRIP1<sup>47</sup> and NEEM-2011-S1<sup>9</sup>) across the 700–1000 CE period have attributed most of the background variation to non-volcanic sources. Annual mean volcanic sulfate deposition across this period was only  $1.0 \text{ kg km}^{-2} \text{ yr}^{-1}$  of sulfate and  $2.1 \text{ kg km}^{-2} \text{ yr}^{-1}$  of sulfate for NGRIP1 and NEEM-2011-S1 respectively. We therefore revised existing reconstructions of volcanic sulfate deposition, now attributing long-term background variations of sulfur as volcanic in origin (see Methods). As a result, we were able to reconstruct overall higher volcanic sulfate deposition rates for NGRIP1 ( $2.4 \text{ kg km}^{-2} \text{ yr}^{-1}$  of sulfate) and NEEM-2011-S1 ( $4.1 \text{ kg km}^{-2} \text{ yr}^{-1}$  of sulfate) (Fig. 6b). Additionally, we reconstruct new volcanic sulfate depositional records from NGRIP2, B19, TUNU2013, and EGRIP (see Fig. 6c), thus doubling the number of ice-core sulfate records from Greenland currently used in reconstructions of volcanic forcing (i.e., by PMIP4) during the Medieval period<sup>35</sup>.

Differences between the analyzed ice cores, with the same events not detected in all ice cores in some instances, may mostly be attributed to the location and elevations of the drill sites (e.g., TUNU2013 and B19 are

**Fig. 5 | Hrafnkatla episode.** **a** Non-sea-salt Sulfur (nss-S) from TUNU2013 ice core and associated insoluble particle record (5–10  $\mu\text{m}$ ) across the period 742–768 CE. Targeted tephra sample (gray shading) and sulfur isotope (green shading) locations (which were screened for tephra) are shown, with the geochemically confirmed occurrences of cryptotephra indicated by red circles; **b** Measured  $\delta^{34}\text{S}$  (‰) and sulfur concentrations versus time recorded in the TUNU2013 ice core; **c** Measured  $\Delta^{33}\text{S}$  (‰) and sulfur concentrations versus time recorded in the TUNU2013 ice core. Blue shading indicates stratospheric  $\Delta^{33}\text{S}$  range ( $0.0 \pm 0.2\text{‰}$ ); **d** Non-crustal thallium (Nc-Tl), non-crustal bismuth (Nc-Bi) and non-sea-salt chlorine (Nss-Cl) record for TUNU2013 ice core. A pronounced enrichment can be observed at the beginning of the Hrafnkatla episode.



700–800 m lower than EGRIP and NGRIP) as these will subject the sites to both different atmospheric circulation and different emission sensitivities towards major volcanic source regions.

## Discussion

Previous suggestions that the period 700–1000 CE was a time of quiescence are not supported by the proximal Icelandic geological records or the Greenland ice-core records. Our application of a multi-proxy geochemical toolkit has revealed heightened volcanic activity from several Icelandic volcanic systems and includes both long-lasting, multi-centennial episodes such as the Icelandic Active Period (IAP) (751–940 CE) and short-lived episodes such as the Hrafnkatla episode (751–763 CE). Both are characterized by prolonged and elevated enrichments of volcanic metals (Tl, Bi) and volatiles (F, Cl, S).

Within Antarctic ice cores, a pronounced elevated halogen and metal enrichment lasting 192 years (~17.7 ka) was attributed to regional West Antarctic volcanism<sup>23,30,48</sup>. Mason et al.<sup>30</sup> suggested that the long-lasting excessive deposition of these volatile species is indicative of a proximal eruption, with magma source chemistry, eruptive processes, and plume transport also contributing to the signature within the ice. Whilst a great deal is still unknown about the behavior of many volatiles during transport, prolonged stratospheric transport (i.e., from a distal eruption) is likely to result in greater loss due to scavenging, and thus reduced or negligible deposition on polar ice sheets. Modern plume and ground-based

measurements of the Hawaiian Kilauea 2018 volcanic eruption support this, with ref. 49 observing a decrease in atmospheric burdens of HF, HCl, and volatile metals with distance from the source due to their solubility. Owing to this decay, and the proximity of Iceland to our Greenland ice-core sites (~1000–1500 km), we suggest that in the Greenland ice cores this metal signature could be used as an indicator for Icelandic eruptions in the absence of cryptotephra. These trace metals are now routinely analyzed over the entire length of deep ice cores and thus are readily available for improved source attribution of volcanic signatures within ice cores<sup>33,27</sup>.

Across the IAP, we propose the prolonged elevated concentrations of volcanic volatiles and volatile metals that are observed can best be explained by continuous volcanic activity dominated by several Icelandic sources (Katla, Bárðarbunga-Veiðivötn, and Grímsvötn). This is supported by the general increased eruption frequency from these systems, with Katla producing 10 times more tephra volume between 750 and 950 CE compared to time-periods before and after<sup>15</sup>. Based on proximal geological and regional glaciochemical records, we postulate that eruptions across the IAP likely encompassed a wide range of volcanic eruption types, involving explosive stratospheric eruptions as well as prolonged fissure and flood basalt eruptions and quiescent degassing. This includes, for example, the long-lasting Hallmundarhraun lava flow, which occurred between 880 and 910 CE, and is considered the third largest effusive eruption since the settlement of Iceland (~877 CE) with an estimated erupted volume of up to 4 km<sup>3</sup><sup>50</sup>.

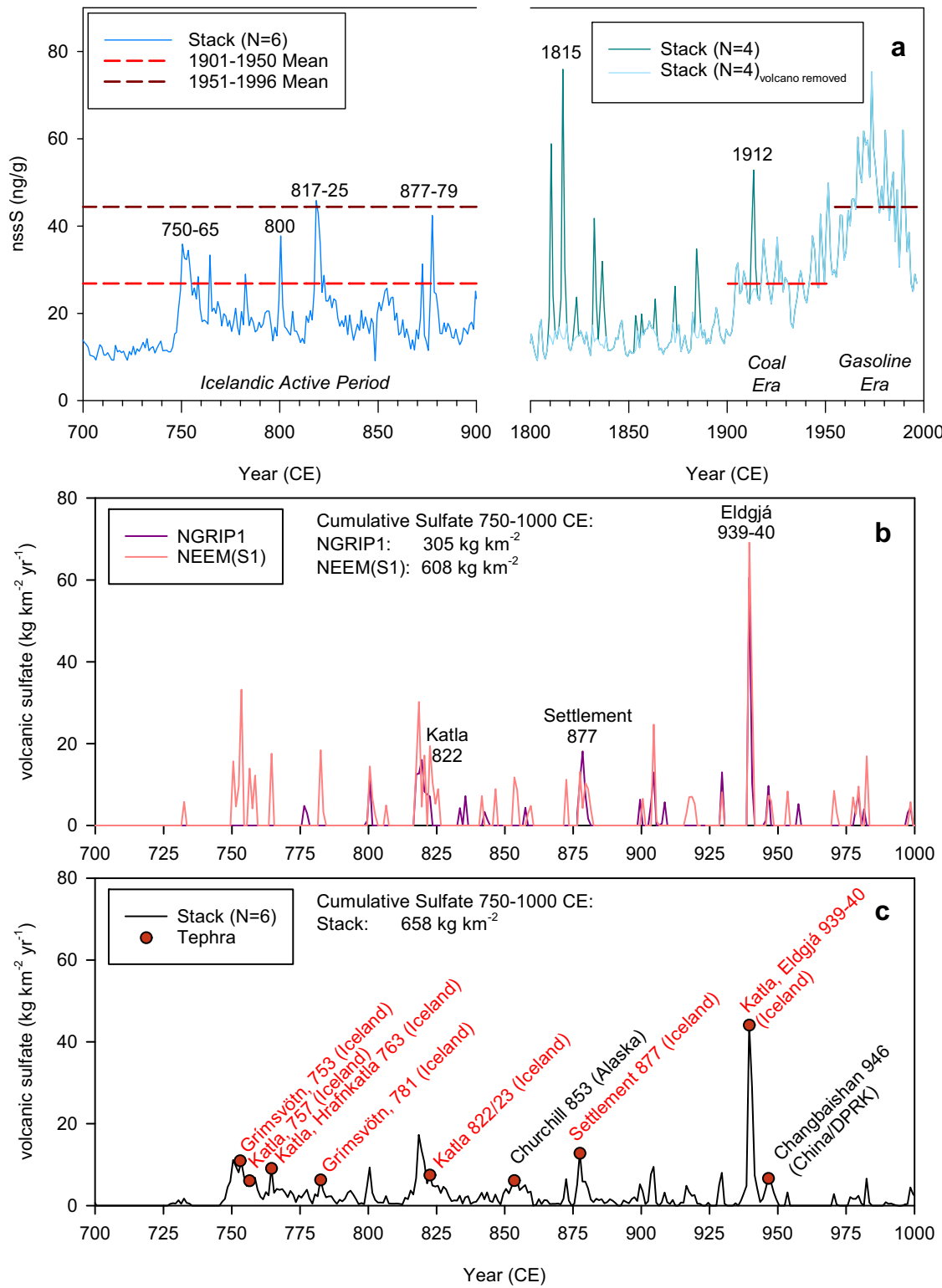


**Fig. 6 | Volcanic sulfate deposition in Greenland ice cores.** **a** Nss-S (stack  $N=6$ ) across the period 700–900 CE and 1800–2000 CE (stack  $N=4$ ). Mean nss-S for the periods 1901–1950 (red dashed line) and 1951–1996 (brown dashed line) are shown for comparison; **b** Annual volcanic sulfate deposition from NGRIP1<sup>47</sup> (purple line) and NEEM-2011-S1<sup>49</sup> (red line) across the period 700–1000 CE; **c** Annual volcanic sulfate

deposition (this study) using a stack ( $N=6$ ) of Greenland ice cores, where calculated cumulative volcanic sulfate for the period 750–1000 CE is greater ( $658 \text{ kg km}^{-2}$ ) compared to  $305 \text{ kg km}^{-2}$  and  $608 \text{ kg km}^{-2}$  for NGRIP1 and NEEM-S1 respectively. Tephra occurrences with confidently attributed sources throughout this period are indicated by the red circles. A comprehensive overview can be found in ref. 20.

Overall, as supported by S isotopes, a large fraction of these aerosol emissions remained predominantly in the troposphere and lowermost stratosphere. This strong and long-lasting tropospheric S contribution led to the estimate of volcanic sulfate deposition in Greenland across this 300-year

period being revised and increased by a factor of 2 (see Fig. 6b, c), thereby challenging the notion of this being a Medieval Quiet Period. Previous underestimations in volcanic sulfate may largely stem from assumptions and conservative approaches used in the detection of volcanic events within

the ice-core records. Prior calculations of volcanic sulfate deposition rates across this 300-year period assumed that the background levels of sulfate in the ice were not volcanic in origin or time variable<sup>9,46,47</sup>. This is inherently linked to the tailoring of detection methods<sup>2,10,51</sup> towards the isolation of short-lived stratospheric perturbing volcanic signals, as these eruptions have typically been associated with stronger climatic impacts on account of the longer residence time of the aerosols within the atmosphere<sup>1,2</sup>. Consequently, the 939 CE Icelandic Eldgjá eruption<sup>28</sup> was identified as the only large eruption across this period, which when accompanied by the relative stability of solar activity across the period 700–1000 CE, subsequently resulted in the period being considered one of quiescence.

Therefore, our revised estimates across this 300-year period, with the inclusion of a long-lasting tropospheric S contribution, have important implications for climate model simulations, such as those from PMIP3 and PMIP4, which use the year 850 CE as the start of the *past1000* simulations covering the pre-industrial millennium (850–1849 CE)<sup>3,4</sup>. These models use only stratospheric volcanic forcing where the tropospheric aerosols are not included, in contrast to historic climate simulations (starting in 1850 CE), which also include tropospheric aerosol forcing.

The role of tropospheric volcanic aerosols in Earth's system should not be neglected. These aerosols not only have direct impacts (i.e., reflection of incoming radiation and surface cooling<sup>52</sup>), but can act as ice-nucleating particles and cloud condensation nuclei, thereby influencing cloud properties and the hydrological cycle<sup>53</sup>. Despite the importance of tropospheric aerosols, little is known about pre-industrial concentrations, a time when the atmosphere showed greater sensitivity towards tropospheric volcanic aerosol inputs (e.g., from quiescent degassing) due to the absence of anthropogenic aerosols<sup>54,55</sup>. Developing a baseline of pre-industrial sulfuric aerosol concentrations would therefore help constrain uncertainties in radiative forcing estimates which are used in climate model simulations.

These ongoing uncertainties and different aerosol baseline conditions during the pre-industrial era have presented challenges when assessing the climate impacts of prolonged volcanic episodes. Here, we further investigate the Hrafnkatla episode, as this marks the onset of the IAP and this abrupt shift in background sulfate, by comparing forcing reconstructions to palaeoenvironmental records from the North Atlantic region where they are abundant and well-dated.

Due to atmospheric circulation patterns, which confine aerosols from high-latitude volcanic eruptions to their respective hemispheres, the climatic impacts of large Icelandic eruptions are more spatially limited than those of tropical eruptions of a similar magnitude. Here, we consider climatic impacts to be those which perturb the system on a seasonal to multi-decadal time scale. The climatic impacts associated with the Hrafnkatla event (the stratospheric eruption which marks the end of Hrafnkatla episode in 762 CE) are generally comparable to other large Icelandic volcanic eruptions such as Eldgjá 939 CE and Laki 1783 CE, with strong winter cooling anomalies across Europe<sup>28,56,57</sup> and perturbations to the hydrological cycle<sup>56,58–60</sup>. At the onset of the Hrafnkatla episode in 751 CE, a cooling signature is recorded in two speleothem records from central Europe (Milandre cave, Switzerland<sup>61</sup> and Spannagel cave, Austria<sup>62,63</sup>), and is most pronounced (up to 1 °C) at around 762–763 CE (see Fig. 7d). These records have a high-resolution (~2 years per sample) and age error of around  $\pm 16$  years (1.s.d) across the study period. Although several processes may govern the isotopic values in speleothems (i.e., climatic and post-depositional), these archives have been shown to reliably capture past climate variability with a demonstrated sensitivity to the post-climatic effects of volcanic eruptions<sup>61</sup>.

Historical records cite the winters of the same and subsequent years of this pronounced cooling anomaly (762–764 CE) among the harshest of the Common Era, with widespread frost and ice, crop failures, and famines documented from Ireland to the Black Sea<sup>64–66</sup> (see Fig. 2). Indeed, the first-hand eyewitness account of Theophanes the Confessor documents an extremely severe winter in the area of the Black Sea and the Bosphorus from October 763 CE to February 764 CE and describes that “in early October [763 CE], there was very bitter cold, not only in our land, but even more so to

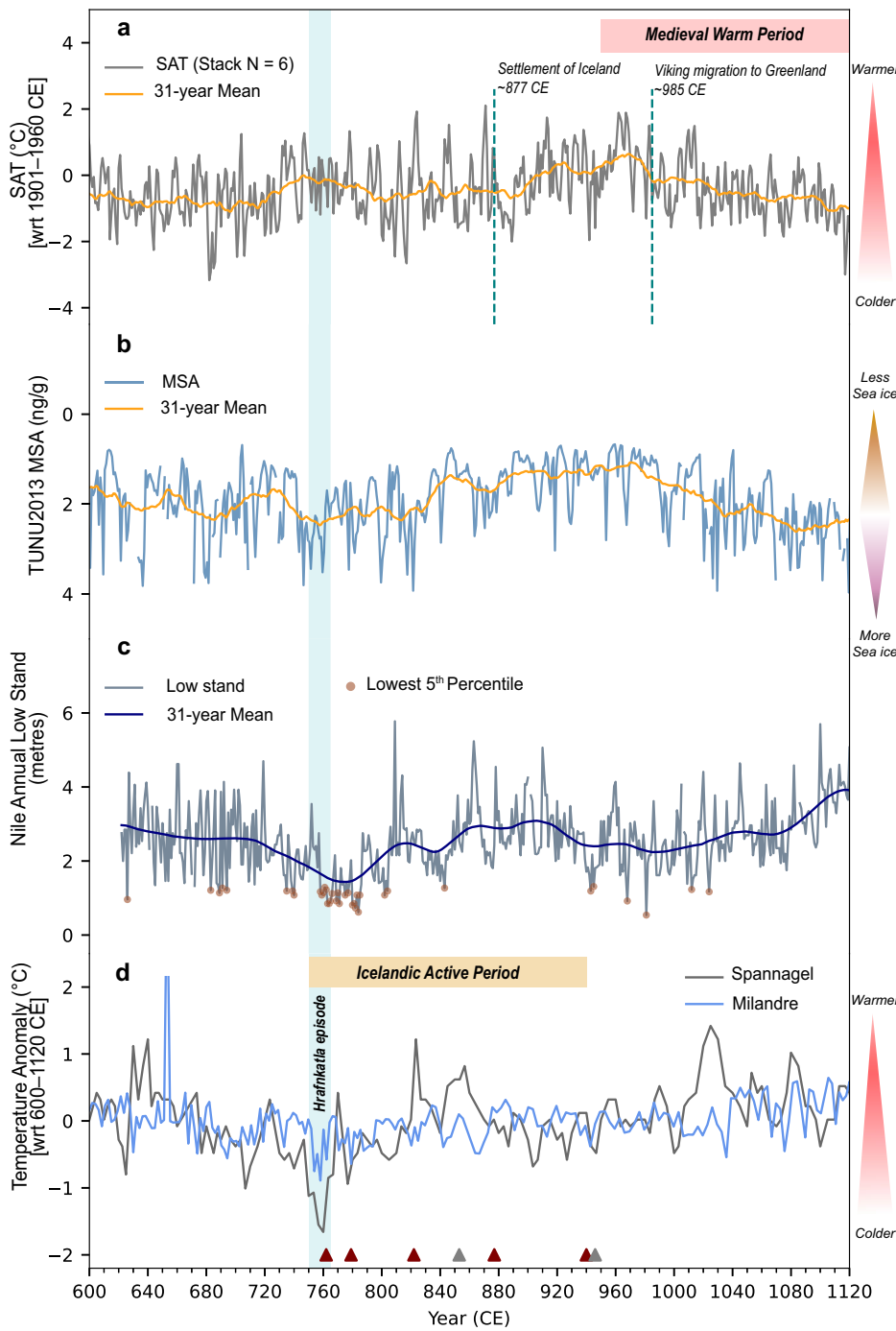
the east, the north, and the west, so that on the north coast of the Pontos [the Black Sea] to a distance of 100 miles the sea froze [...] In the month of February [764 CE] this ice was [...] split up into many different mountain-like sections. [...] One of the icebergs struck the jetty of the Acropolis [of Constantinople] and crushed it”<sup>67–69</sup>. These harsh conditions documented across Europe coincide with a period of extreme annual low stand values of the river Nile (20 of the 52 lowest 5<sup>th</sup> percentiles occurred between 750 to 790 CE)<sup>70</sup> (Fig. 7c). The flow of the river Nile is highly sensitive to shifts in the Intertropical Convergence Zone (ITCZ), with the headwaters of the Nile located in the equatorial regions. The ITCZ is displaced southward in response to the high atmospheric burden of sulfate aerosols and subsequent cooling within the Northern Hemisphere atmosphere following high-latitude eruptions, resulting in varied precipitation patterns in the equatorial regions and reduced stream flow of the Nile<sup>56,71,72</sup>. The low flow following these short-lived high-latitude eruptions is of short duration (i.e., the year after the eruption), and therefore, the clustering of extreme annual low stand values occurring during and following the Hrafnkatla episode may suggest a different, more persistent tropical hydroclimatic response following prolonged volcanic emissions as was the case during the 20th century which was dominated by anthropogenic sulfur emissions<sup>73–77</sup>. Climate models may provide further insight, as they can better explore the mechanisms and feedbacks following prolonged volcanic emissions.

In contrast to many historic large eruptions, no major summer cooling anomaly is recorded in Northern Hemisphere tree-ring reconstructions in the year following the explosive stratospheric end-phase of the Hrafnkatla episode (i.e., 764 CE)<sup>78–80</sup>. The cause for this absence of a summer cooling anomaly is unknown; however, given that the explosive Hrafnkatla event followed a 12-year period of sustained aerosol emissions, increased background aerosol concentrations may have modified the climatic response. Arctic sea-ice plays an important role in amplifying and sustaining climatic responses to large explosive volcanic eruptions, and typically, following an explosive volcanic eruption there is an expansion in sea-ice<sup>81–83</sup>. In contrast, methanesulphonic acid (MSA) concentrations (a proxy for sea-ice) from the TUNU2013 Greenland ice core<sup>84</sup> (Fig. 7b) show no clear indication of a strong sea-ice expansion around the 760s CE. They do however, indicate a general reduction in Arctic sea-ice across the IAP, coincidental with an increase in surface air temperature, peaking in the late 10th century (Fig. 7a). This transition into a North Atlantic Medieval Warm Period (MWP) coincided with the Viking expansion across the Arctic region to settle first in Iceland (~877 CE) and then in southern Greenland (~985 CE)<sup>85,86</sup>. Arguably, these warmer temperatures and ice-free conditions may have facilitated such an expansion. Ultimately, this is an area that requires further research, with continued uncertainties regarding the climatic response and feedbacks associated with prolonged volcanic episodes, particularly during the pre-industrial era.

In conclusion, our application of a multi-proxy geochemical toolkit has revealed that the period 751–940 CE was a time of heightened Icelandic volcanic activity, which commenced with the Hrafnkatla episode in 751 CE. This is in contrast to previous suggestions of the period 700–1000 CE being a time of quiescence, as indicated by global radiative aerosol forcing estimates. This period was characterized by heavy metal and halogen enrichments, with these species most pronounced at the time of local Icelandic eruptions. We have therefore postulated that both heavy metals and halogens can be used as distinct tracers of Icelandic volcanic eruptions within the Greenland ice core records and aid in discerning the source in the absence of cryptotephra. Through our attribution of several volcanic signals within the Greenland ice-core records to Icelandic volcanic systems, we have been able to resolve existing mismatches between these regional records and proximal geological records. Our revision of volcanic sulfur deposition across this period identified a greater tropospheric contribution of sulfate aerosols, which is currently not considered in existing volcanic forcing estimates. We found that the explosive stratospheric end-phase of the Hrafnkatla episode coincided with a strong winter cooling anomaly throughout Europe and could be considered as a likely cause, owing to the absence of major tropical eruptions during this time period. However, unlike other large explosive

**Fig. 7 | Palaeoenvironmental and proxy records**

**600–1120 CE.** a Surface air temperature (SAT [ $^{\circ}\text{C}$ ])<sup>[31]</sup> inferred from a  $\delta^{18}\text{O}$  stack ( $N = 6$ ) of Greenland ice cores with 31-year mean (yellow line). The timing of the Hrafnkatla episode (blue) is shown, alongside the onset of the Medieval Warm Period (red) and the settlement of Iceland and Greenland (green dashed line); b TUNU2013 MSA<sup>[84]</sup> with 31-year mean (yellow line). Outliers have been detected and removed with a threshold of 1.5 times the Interquartile range; c Nile annual low stand<sup>[70]</sup> with 31-year mean (dark blue line), with the lowest 5th percentiles marked by brown circles; d Spannagel cave<sup>[62,63]</sup> (gray line) and Milandre cave (blue line)[this study] speleothem temperature anomalies [ $^{\circ}\text{C}$ ] with reference to mean annual air temperature (MAAT) across the 600–1120 CE period are shown. Icelandic (red triangles) and NHET (gray triangles) volcanic eruptions during the Icelandic Active Period (yellow) are shown.



volcanic eruptions, no major summer temperature anomaly has been observed thus far. Finally, we suggest that more research into prolonged volcanic episodes, such as the IAP and Hrafnkla episode, is required due to the uncertainties in the associated climate feedbacks to sustained tropospheric aerosol emissions, especially during the pre-industrial period. Ultimately, resolving these uncertainties will be of particular importance when investigating other time intervals such as the last deglaciation to early Holocene, where evidence suggests long-lasting volcanic episodes occurred frequently, with some lasting up to 70 years<sup>6,24</sup>.

## Methods

## Ice-core analysis

Information regarding the seven Greenland ice-core records used within this study NEEM-2011-S1, NGRIP1, NGRIP2, EGRIP, RECAP, B19, and

TUNU2013) can be found in Supplementary Table 1. Elemental data (including sulfur, chlorine, bismuth, and thallium) for NGRIP2, NEEM-2011-S1, and TUNU2013<sup>9,26,27</sup> ice cores were utilised alongside new measurements of these elements in the B19 ice core (78.00°N 36.40°E, 150.4 m depth, 2234 m a.s.l.)<sup>87</sup>. All data from these four ice cores were obtained through continuous flow analysis (CFA) coupled to two inductively coupled plasma mass spectrometers (ICP-MS, Element2, Thermo Scientific) at the Desert Research Institute, USA (DRI), providing a simultaneous determination of a broad spectrum of elements at a sub-annual resolution<sup>23</sup>. Additional sulfate ( $\text{SO}_4^{2-}$ ), chloride ( $\text{Cl}^-$ ), and fluoride ( $\text{F}^-$ ) measurements for EGRIP and NGRIP1 were undertaken at the Alfred Wegner Institute, Germany (AWI), and Physics of Ice, Climate and Earth, Denmark (PICE), respectively, using ion chromatography. NGRIP1 had been sampled discretely at 5 cm depth resolution; EGRIP samples were taken during the CFA

analyses at the University of Bern using a fraction collector with a nominal depth resolution of  $\sim 6$  cm<sup>88</sup>. For the determination of anionic species in EGRIP, a two-channel Dionex ICS 5000+ reagent-free HPIC system (Thermo Fisher) with a Dionex IonPac AS18-Fast-4  $\mu$ m analytical column was used. Details of the entire sampling procedure and analytical conditions are described in detail in ref. 89. Between 700 and 1000 CE the time resolution is about 0.5 years in EGRIP. For quantification of ionic species in NGRIP1 a two-channel Dionex 500 microbore ion chromatograph was used<sup>47,90,91</sup> resulting in a time resolution of about four samples per year during the first millennium CE. In addition, methanesulphonic acid (MSA) was measured at DRI continuously over the TUNU2013 ice core using an electrospray triple-quad mass spectrometer (ESI-MS-MS)<sup>84</sup> alongside stable water isotope ratios ( $\delta^{18}\text{O}$ ), determined using a cavity ring-down water isotope analyzer (L2130-i, Picarro Inc)<sup>92</sup>. All parameters measured for each ice core and used within this study can be found in Supplementary Table 1.

### Ice-core data processing

We estimated non-sea-salt sulfur (nss-S) concentrations by correcting total S concentrations for the sulfur contribution from sea salt using co-registered Na concentrations as a sea salt tracer and assuming a sulfur to sodium mass ratio in bulk sea water of 0.084<sup>93</sup>. Similarly, we estimated non-sea-salt chlorine (nss-Cl) concentrations by correcting total Cl concentrations for the chlorine contribution from sea salt using co-registered Na concentrations as a sea salt tracer and assuming a chlorine to sodium mass ratio in bulk sea water of 1.796<sup>94</sup>. To calculate the non-crustal fractions (nc-Tl and nc-Bi) and enrichment factors (Tl-EFCe and Bi-EFCe, see Supplementary Fig. 9), we used cerium (Ce) as a conservative tracer for mineral dust and the “mean continental crust” Tl/Ce ratio of 0.01172 and Bi/Ce of 0.00198, respectively<sup>95</sup>. Ce concentrations were scaled by a factor of 1.7 to account for an under-recovery of Ce (of 60%) during the continuous-flow analysis at the Desert Research Institute, whereas recovery was  $\sim 100\%$  for both Tl and Bi<sup>96</sup>.

### Targeted sampling

CFA measurements of insoluble particles at two size fractions (2.6–4.5  $\mu\text{m}$  and 4.5–9.5  $\mu\text{m}$ ) were used alongside peaks in sulfur to assist with isolating events and sampling for tephra. Particle measurements were undertaken using an inline Abakus® laser particle counter<sup>97</sup> during the CFA analyses at DRI. Although the particle concentrations alone cannot be considered as a direct proxy for tephra, the application of this approach, based on the exact stratigraphic co-registration of insoluble particulates and volcanic volatiles in the polar ice cores, has proven highly successful for detecting cryptotephra layers<sup>19,33,98–103</sup>. One 11 cm-long sample was obtained for tephra analysis from the RECAP ice core between 297.44–297.55 m for which a non-targeted continuous sampling approach was followed as described by ref. 104.

### Ice-core chronologies

The NS1-2011<sup>26</sup> and DRI\_NGRIP2<sup>27</sup> chronologies are used within this study. Both chronologies were constructed through annual layer counting of seasonally varying impurity tracers constrained by well-dated stratigraphic markers such as historic volcanic eruptions, volcanic dust veils, and solar energetic particle events (see Supplementary Tables 2, 3). Dating uncertainty in both chronologies during the period 700–1000 CE is  $\pm 2$  years. This is supported by the occurrence of short-lived cosmogenic nuclide events in 774 CE and 993 CE, which are observed in both the ice core and tree-ring records<sup>26,105,106</sup> and by exact matches of dendrochronologically dated volcanic eruptions and corresponding ice-core tephra identifications in 822/823 CE<sup>33,105</sup> and 946/947 CE<sup>28</sup>. Both chronologies are within errors consistent with the GICC21 chronology<sup>107</sup>, but are more precise during the period 700–1000 CE because of the additional age constraints. To transfer the age of the RECAP ice core tephra sample (available on the GICC05 chronology<sup>108</sup>) to the NS1-2011 chronology, we used an age transfer of  $+7$  years following ref. 26.

### Cryptotephra analysis

Targeted tephra samples were obtained for 11 volcanic events from TUNU2013, B19, and RECAP ice cores and analyzed at Queen’s University Belfast, UK (QUB); University of Bern, Switzerland (UniBe); and the University of Edinburgh, UK (Edin), respectively (see Supplementary Data). The targeted sampling approach allowed us to sample comparably large cross sections of archived ice ranging between 16.5  $\text{cm}^2$  (RECAP) and 15  $\text{cm}^2$  (B19) thus increasing the chance of retrieving greater abundances of tephra shards. In addition, samples that were analyzed for S isotopes were also centrifuged prior to analysis, facilitating the screening for cryptotephra. The method for the preparation for tephra identification and geochemical analysis of samples analyzed at QUB and Edin can be found in ref. 98 and ref. 104 respectively, and secondary standards for analyses obtained in this study can be found in the Supplementary Data. The preparation of samples for tephra identification and geochemical analysis at UniBe followed a method adapted from several recent papers<sup>109–112</sup> and the full methodology used within this study can be found in Supplementary Methods A. Samples where glass tephra shards were identified were analyzed using Electron probe microanalysis (EPMA) at the Institute of Geological Sciences, University of Bern, Switzerland. The samples were carbon coated prior to major elemental analysis using a JEOL JXA-8200 probe, with operating conditions of an accelerating voltage of 15 kV, beam current of 2 nA, and beam diameter of 5  $\mu\text{m}$ . Secondary standards of Canneto Lami Lava, Lipari and BCR-2G were measured during the analytical session to ensure stability and allow session comparisons. Full details about the operating conditions and secondary standards at UniBe can be found in the Supplementary Data.

Following the filtering of all obtained data to totals  $>90$  wt% and the removal of Cl and  $\text{P}_2\text{O}_5$  (to facilitate correlation with other data sets), the data were normalized to an anhydrous basis following standardised practices<sup>113</sup>. The data were further inspected to remove any outliers, both those occurring from analytical issues (e.g., analysis of the resin) and those which appeared outside of the main population. All raw data can be found in the Supplementary Data. Data were then correlated to published tephra geochemical data, with potential correlations explored graphically. In order to make robust correlations, samples were analyzed alongside proximal material when available, which was obtained in summer 2021/2022 fieldwork. The full preparation method for proximal material and sampling strategy can be found in Supplementary Methods B.

Trace element analysis was conducted on individual glass shards from four ice core and three proximal samples covering the period 751–763 CE using laser ablation inductively coupled plasma mass spectrometry (LA-ICP-MS) at St Andrews Isotope Geochemistry lab, UK (StAiG). Laser ablation used an Applied Spectra RESolution system, featuring a Laurin Technic S155 2-volume cell under a pure He atmosphere (370  $\text{mL min}^{-1}$ ) with supplemental  $\text{N}_2$  (5  $\text{mL min}^{-1}$ ) to improve sensitivity in the ICP-MS. Analyses were undertaken using a 20  $\mu\text{m}$  beam diameter and a laser energy of 3.5  $\text{J cm}^{-2}$  with a 4 Hz repetition rate, 20-s background measurement, and 30-s ablation time. The laser cell gases and ablated sample were mixed with Ar (1  $\text{L min}^{-1}$ ) before being homogenized in a signal smoothing device prior to introduction to an Agilent 8900-QQQ for mass spectrometry. Measurements of glass standards of Old Crow, Sheep Track, and ML3B, and synthetic glass standards of NIST610 and T1G which were used to correct for drift, bracketing measurements, can be found in the Supplementary Data. Samples were normalized using  $\text{Al}_{27}$ , which was determined from the same samples during previous EPMA at the UniBe. A detailed methodology can be found in ref. 114. All raw data can be found in the Supplementary Data.

### Sulfur isotope analysis

The ratio of isotopic  $^{34}\text{S}$ ,  $^{32}\text{S}$ , can be used to determine the origin of the sulfate (i.e., marine or volcanic)<sup>115–117</sup>. This distinction can be made through the

measurement of  $\delta^{34}\text{S}$  (defined as,

$$\delta^x\text{S} = \left( \left( ^x\text{S} / ^{32}\text{S} \right)_{\text{sample}} / \left( ^x\text{S} / ^{32}\text{S} \right)_{\text{reference}} \right) - 1 \quad (1)$$

where  $x$  is 33 or 34). Marine sulfate typically has values between 16–20‰, whilst volcanic isotopic values are closer to zero<sup>117–121</sup>. By measuring the minor isotope,  $^{33}\text{S}$ , one can assess Mass-independent Fractionation (MIF) by calculating  $\Delta^{33}\text{S}$  (defined as,

$$\Delta^{33}\text{S} = \delta^{33}\text{S} - ((\delta^{34}\text{S} + 1)^{0.515} - 1) \quad (2)$$

$\Delta^{33}\text{S}$  isotopic values can be used to determine whether sulfate aerosol formation occurred in the stratosphere (i.e., above the ozone layer) since UV photochemical reactions generate MIF and non-zero  $\Delta^{33}\text{S}$ <sup>10,122–124</sup>. As a result, sulfur deposited over the ice sheet that has reached the stratosphere has  $\Delta^{33}\text{S} \neq 0$ . Due to the ozone layer, which filters out radiation of the specific wavelength that causes MIF, the sulfate which remains in the troposphere/lowermost stratosphere is not exposed to UV radiation. Therefore, Mass-Dependent Fractionation (MDF) is generated and tropospheric/lowermost stratospheric sulfate has a  $\Delta^{33}\text{S}$  isotopic value that is equal to zero. Through these different fractionation processes, it is possible to distinguish stratospheric sulfate from tropospheric/lowermost stratospheric sulfate and provide an insight into the explosivity and plausible plume heights of past eruptions.

We undertook S isotopic measurements on samples from TUNU2013 across an elevated period of sulfate concentrations. TUNU2013 was continuously sampled at a 3 cm depth resolution (cross sections of 7 cm<sup>2</sup>) between 740 and 765 CE for sulfur isotope analysis at the University of St Andrews Isotope Geochemistry Laboratory (StAiG), UK. The detailed methodology can be found in the methodology of ref. 37. Briefly, the sulfate concentration of each sample was first determined by ion chromatography using a Metrohm 930 Compact IC Flex. Sulfate was then extracted from the sample using column chemistry and triple sulfur isotopes ( $^{32}\text{S}$ ,  $^{33}\text{S}$ , and  $^{34}\text{S}$ ) were subsequently measured using a Neptune Plus Multi-Collector-ICPMS<sup>125</sup>. These measurements were conducted alongside an established secondary standard (Switzer Falls<sup>126</sup>) and procedural blanks. The procedural blank values ( $0.18 \pm 0.08$  nmol S,  $\delta^{34}\text{S} = 6.8 \pm 4.3\text{‰}$ , 1 s.d.,  $n = 11$ ) were used to correct all measured ratios. The  $\delta^{33}\text{S}$  and  $\delta^{34}\text{S}$  values were used to calculate  $\Delta^{33}\text{S}$ . The external reproducibility of the secondary standards run alongside these samples (0.19‰, 0.08‰, and 0.09‰ for  $\delta^{34}\text{S}$ ,  $\delta^{33}\text{S}$ , and  $\Delta^{33}\text{S}$  respectively, 1 s.d.,  $n = 9$ ) is used as the reported uncertainty on isotope ratios. For some samples there was only enough sulfate for a single isotope measurement, and thus the uncertainty on these samples is slightly elevated and was calculated from the external reproducibility of the secondary standard when only one replicate was considered (0.22‰, 0.1‰, and 0.1‰ for  $\delta^{34}\text{S}$ ,  $\delta^{33}\text{S}$  and  $\Delta^{33}\text{S}$  respectively, 1 s.d.,  $n = 9$ ). The isotope data can be found in the Supplementary Data. Following the approach of ref. 38, Gautier et al.<sup>127</sup>, we used isotope mass balance to solve for the sulfur isotopic composition of volcanic sulfate (see Supplementary Fig. 7) using the following equation:

$$\delta^x\text{S}_{\text{volc}} = \frac{(\delta^x\text{S}_{\text{meas}} - f_{\text{background}} \cdot \delta^x\text{S}_{\text{background}})}{f_{\text{volc}}} \quad (3)$$

where  $\delta^x\text{S}_{\text{meas}}$  is the measured isotopic value,  $f_{\text{background}}$  is the fraction of background sulfate ( $f_{\text{background}} = \text{sulfate concentration of background} / \text{total sulfate}$ ),  $f_{\text{volc}}$  is the fraction of volcanic sulfate ( $f_{\text{volc}} = 1 - f_{\text{background}}$ ), and  $\delta^x\text{S}_{\text{background}}$  is the isotopic composition of the background sulfate. We use the mean and standard deviation of sulfate concentration and sulfur isotope composition from 13 TUNU2013 non-volcanic background samples analyzed throughout the Common Era to calculate  $f_{\text{background}}$  and  $\delta^x\text{S}_{\text{background}}$ . Uncertainties on this calculation are propagated using Monte Carlo simulations, and only samples with more than 57% volcanic sulfate are plotted, similar to that suggested by ref. 127.

## Volcano detection

Several statistical methods have been applied in previous studies to the ice-core sulfate records to isolate volcanic events from the background signal<sup>128,129</sup>. These methods often use running medians of multi-decadal lengths for the separation of time-variant volcanic and background sulfate (a combination of time invariant marine and volcanic contributions). Their application has proven successful in the detection of climate impacting (medium and large sized) volcanic events, but ultimately has resulted in an underestimation in the total amount of volcanic sulfate. Within this study, we therefore adjusted the previous methods<sup>9,128,129</sup>, across the NEEM-2011-S1, NGRIP1, NGRIP2, EGRIP, B19, and TUNU2013 ice core records, as follows: a 91-year Running Median (RM) was used on the annually averaged nss-S record on periods unaffected by strong changes in volcanic background emissions (i.e., 300–700 CE for all cores but B19, for which 950–1250 CE was used) to estimate the natural background sulfate levels<sup>2</sup>; a Median of Absolute Deviation (MAD), calculated from the RM, was used in peak detection. As with the calculation of the RM, the MAD for the period before (i.e., 300–700 CE and 950–1250 CE for B19) was used. A peak was considered volcanic if it passed the upper threshold ( $K = 3$ , estimated as RM plus  $3^* \text{MAD}$ ). The duration of the event was determined when it passed the lower threshold ( $K = 1$ , estimated as the RM plus  $1^* \text{MAD}$ ). These upper and lower thresholds were selected by validation on well-known historic eruptions<sup>3</sup>; volcanic peaks were then removed to calculate the non-volcanic background (S RRMi). To further calculate the amount of sulfate deposited, S RRMi (from 300–700 CE and 950–1250 CE for B19) was subtracted from the average annual nss-S and then multiplied by the accumulation rate of the drill site<sup>4</sup>; finally, cumulative volcanic sulfate deposition was calculated for each event by summing the sulfate deposited across the total duration of the event.

## Temperature reconstruction for Milandre cave (Switzerland) 600–1200 CE

The Milandre cave (see Fig. 2) temperature reconstruction is based on oxygen isotope measurements ( $\delta^{18}\text{O}$ ) of speleothem calcite and the data can be found in the Supplementary Data. The statistically significant correlation ( $r^2 = 0.56$ ,  $p = 0.0001$ ) between stalagmite calcite  $\delta^{18}\text{O}$ <sup>61</sup> and historical and instrumental temperature records from western Switzerland<sup>130</sup> allows the development of a transfer function to calculate mean annual air temperatures (MAAT) for the last two millennia for western Switzerland.

## Temperature reconstructions from Greenland $\delta^{18}\text{O}$ stack 600–1120 CE

As a proxy for annual mean surface air temperatures (SAT) over Greenland, we collated published stable oxygen isotope ( $\delta^{18}\text{O}$ ) records across Greenland fulfilling the three selection criteria: continuous coverage between 600 and 1120 CE, with annual time resolution, and dating precision and accuracy better than  $\pm 3$  years. A total of six records met these requirements, from the Dye-3, NGRIP, NEEM, GRIP, EGRIP, and TUNU2013 ice cores<sup>107,131,132</sup>. We then compiled our dataset of these individual  $\delta^{18}\text{O}$  anomaly records (relative to a 1901–1960 reference interval) into a single stack by calculating the arithmetic mean  $\delta^{18}\text{O}$  anomaly for each year. We further apply a 31-year running mean filter to our time series and estimated temperature anomalies, by applying the spatial calibration slope for Greenland of  $1/0.67^\circ\text{C}$  per ‰<sup>133,134</sup>.

## Data availability

NGRIP1 glaciochemical data is available at PANGAEA (<https://doi.org/10.1594/PANGAEA.944172>)<sup>135</sup>. NGRIP1 sulfate data is available from the Physics of Ice, Climate and Earth, University of Copenhagen: [https://www.iceandclimate.nbi.ku.dk/data/2012-12-03\\_NGRIP\\_SO4\\_5cm\\_Plummet\\_et\\_al\\_CP\\_2012.txt](https://www.iceandclimate.nbi.ku.dk/data/2012-12-03_NGRIP_SO4_5cm_Plummet_et_al_CP_2012.txt)<sup>47,136</sup>. NEEM-2011-S1 glaciochemical data is available at PANGAEA (<https://doi.org/10.1594/PANGAEA.940553>)<sup>137</sup> and at the Arctic Data Centre (<https://doi.org/10.18739/A2HX15R7T>)<sup>138</sup>; TUNU2013 glaciochemical and stable isotope data is available at Arctic Data Centre (<https://doi.org/10.18739/A2057CS7S>)<sup>139</sup>; <https://doi.org/10.18739>

A2F18SF79<sup>140</sup>); NGRIP2 glaciochemical data is available at Arctic Data Centre (<https://doi.org/10.18739/A20R9M558>)<sup>141</sup>. Nile River flow data is available at (<https://doi.org/10.1029/2004GL022156>)<sup>70</sup>; Spannagel cave temperature data is available at NOAA (<https://doi.org/10.25921/7d43-qz51>)<sup>142</sup>. Volcanic forcing data is available at the World Data Center for Climate (WDCC) at DKRZ ([https://doi.org/10.26050/WDCC/eVolv2k\\_v3](https://doi.org/10.26050/WDCC/eVolv2k_v3))<sup>143</sup>. For the study period 700–1000 CE additional new data is available: EGRIP ice core ion chromatography data is available at PANGAEA (<https://doi.pangaea.de/10.1594/PANGAEA.966039><sup>144</sup>; <https://doi.pangaea.de/10.1594/PANGAEA.966041><sup>145</sup>); Ice-core concentration records of Na, Cl, S, Ce, Bi, Tl from the B19, TUNU2013, NEEM-2011-S1 and NGRIP2 ice cores in Greenland is available at the Arctic Data Center (<https://doi.org/10.18739/A2BK16R39>)<sup>146</sup>; Tephra geochemical data from identified volcanic events from B19, TUNU2013, and RECAP Greenland ice cores and correlating proximal material between 750 and 940 CE is available at PANGAEA (<https://doi.org/10.1594/PANGAEA.967050>)<sup>147</sup>; Sulfate concentration and sulfur isotope data from Greenland TUNU2013 ice-core samples between 740–765 CE is available at PANGAEA (<https://doi.org/10.1594/PANGAEA.967047>)<sup>148</sup>; Sulfur and volcanic sulfate deposition from 6 ice cores in Greenland 700–1000 CE is available at PANGAEA (<https://doi.org/10.1594/PANGAEA.967071>)<sup>149</sup>). Milandre cave data covering the period 600–1200 CE is available in the Supplementary Data. All additional new data sets included as part of this study can be found in the Supplementary Data.

Received: 7 September 2023; Accepted: 27 March 2024;

Published online: 10 April 2024

## References

1. Robock, A. Volcanic eruptions and climate. *Rev. Geophys.* **38**, 191–219 (2000).
2. Cole-Dai, J. Volcanoes and climate. *Wiley Interdiscip. Rev. Clim. Change* **1**, 824–839 (2010).
3. Jungclaus, J. H. et al. The PMIP4 contribution to CMIP6 - Part 3: the last millennium, scientific objective, and experimental design for the PMIP4 past1000 simulations. *Geosci. Model Dev.* **10**, 4005–4033 (2017).
4. Schmidt, G. A. et al. Climate forcing reconstructions for use in PMIP simulations of the last millennium (v1.0). *Geosci. Model Dev.* **4**, 33–45 (2011).
5. Toohey, M. & Sigl, M. Volcanic stratospheric sulfur injections and aerosol optical depth from 500 BCE to 1900 CE. *Earth Syst. Sci. Data* **9**, 809–831 (2017).
6. Sigl, M., Toohey, M., McConnell, J. R., Cole-Dai, J. & Severi, M. Volcanic stratospheric sulfur injections and aerosol optical depth during the Holocene (past 11 500 years) from a bipolar ice-core array. *Earth Syst. Sci. Data* **14**, 3167–3196 (2022).
7. Marshall, L. R. et al. Large variations in volcanic aerosol forcing efficiency due to eruption source parameters and rapid adjustments. *Geophys. Res. Lett.* **47**, <https://doi.org/10.1029/2020GL090241> (2020).
8. Bradley, R. S., Wanner, H. & Diaz, H. F. The Medieval Quiet Period. *The Holocene* **26**, 990–993 (2016).
9. Sigl, M. et al. A new bipolar ice core record of volcanism from WAIS Divide and NEEM and implications for climate forcing of the last 2000 years. *J. Geophys. Res. Atmos.* **118**, 1151–1169 (2013).
10. Zielinski, G. A. et al. Record of volcanism since 7000 BC from the GISP2 Greenland ice core and implications for the volcano-climate system. *Science* **264**, 948–952 (1994).
11. Abbott, P. M. & Davies, S. M. Volcanism and the Greenland ice-cores: the tephra record. *Earth-Science Reviews* **115**, 173–191 (2012).
12. Bourne, A. J. et al. A tephra lattice for Greenland and a reconstruction of volcanic events spanning 25–45 ka b2k. *Quat. Sci. Rev.* **118**, 122–141 (2015).
13. Cook, E. et al. Volcanism and the Greenland ice cores: a new tephrochronological framework for the last glacial-interglacial transition (LGIT) based on cryptotephra deposits in three ice cores. *Quat. Sci. Rev.* **292**, 107596 (2022).
14. Óladóttir, B. A., Larsen, G. & Sigmarsson, O. Holocene volcanic activity at Grímsvötn, Bárdarbunga and Kverkfjöll subglacial centres beneath Vatnajökull, Iceland. *Bull. Volcanol.* **73**, 1187–1208 (2011).
15. Óladóttir, B. A., Sigmarsson, O. & Larsen, G. Tephra productivity and eruption flux of the subglacial Katla volcano Iceland. *Bull. Volcanol.* **80**, 1–16 (2018).
16. Gudmundsdóttir, E. R., Larsen, G., Björck, S., Ingólfsson, Ó. & Striberger, J. A new high-resolution Holocene tephra stratigraphy in eastern Iceland: Improving the Icelandic and North Atlantic tephrochronology. *Quat. Sci. Rev.* **150**, 234–249 (2016).
17. Thordarson, T. & Larsen, G. Volcanism in Iceland in historical time: Volcano types, eruption styles and eruptive history. *J. Geodyn.* **43**, 118–152 (2007).
18. Thordarson, T. & Höskuldsson, Á. Postglacial volcanism in Iceland. *Jökull* **58**, 228 (2008).
19. Plunkett, G., Sigl, M., McConnell, J. R., Pilcher, J. R. & Chellman, N. J. The significance of volcanic ash in Greenland ice cores during the Common Era. *Quat. Sci. Rev.* **310**, 107936 (2023).
20. Coulter, S. E. et al. Holocene tephras highlight complexity of volcanic signals in Greenland ice cores. *J. Geophys. Res. Atmos.* **117**, D21 (2012).
21. Legrand, M. Ice–core records of atmospheric sulphur. *Philos. Trans. R. Soc. London* **352**, 241–250 (1997).
22. Self, S., Coffin, M. F., Rampino, M. R. & Wolff, J. A. Large igneous provinces and flood basalt volcanism. in *The Encyclopedia of Volcanoes*, 441–455 (Academic Press, 2015).
23. McConnell, J. R. et al. Synchronous volcanic eruptions and abrupt climate change ~17.7 ka plausibly linked by stratospheric ozone depletion. *Proc. Natl. Acad. Sci.* **114**, 10035–10040 (2017).
24. MacLennan, J., Jull, M., McKenzie, D., Slater, L. & Grönvold, K. The link between volcanism and deglaciation in Iceland. *Geochem. Geophys. Geosyst.* **3**, 1–25 (2002).
25. Sinton, J., Grönvold, K. & Sæmundsson, K. Postglacial eruptive history of the Western Volcanic Zone, Iceland. *Geochem. Geophys. Geosyst.* **6**, 12 (2005).
26. Sigl, M. et al. Timing and climate forcing of volcanic eruptions for the past 2,500 years. *Nature* **523**, 543–549 (2015).
27. McConnell, J. R. et al. Lead pollution recorded in Greenland ice indicates European emissions tracked plagues, wars, and imperial expansion during antiquity. *Proc. Natl. Acad. Sci.* **115**, 5726–5731 (2018).
28. Oppenheimer, C. et al. The Eldgjá eruption: timing, long-range impacts and influence on the Christianisation of Iceland. *Clim. Change* **147**, 369–381 (2018).
29. McConnell, J. R. et al. Hemispheric-scale heavy metal pollution from South American and Australian mining and metallurgy during the Common Era. *Sci. Total Environ.* **912**, <https://doi.org/10.1016/j.scitotenv.2023.169431> (2024).
30. Mason, E., Edmonds, M. & McConnell, J. R. Volatile trace metals deposited in ice as soluble volcanic aerosols during the 17.7 ka eruptions of Mt Takahe, West Antarctic Rift. *Front. Earth Sci.* **10**, 1002366 (2022).
31. Óladóttir, B. A., Larsen, G. & Sigmarsson, O. Deciphering eruption history and magmatic processes from tephra in Iceland. *Jökull* **62**, 21–38 (2012).
32. Óladóttir, B. A., Larsen, G., Thordarson, T. & Sigmarsson, O. The Katla volcano S-Iceland: Holocene tephra stratigraphy and eruption frequency. *Jökull* **55**, 53–74 (2005).
33. Plunkett, G. et al. Smoking guns and volcanic ash: The importance of sparse tephras in Greenland ice cores. *Polar Res.* **39**, <https://doi.org/10.33265/polar.v39.3511> (2020).

34. Schmid, M. M., Dugmore, A. J., Vésteinsson, O. & Newton, A. J. Tephra isochrons and chronologies of colonisation. *Quat. Geochronol.* **40**, 56–66 (2017).

35. Grönvold, K. et al. Ash layers from Iceland in the Greenland GRIP ice core correlated with oceanic and land sediments. *Earth Planet. Sci. Lett.* **135**, 149–155 (1995).

36. Zielinski, G. A., Mayewski, P. A., Meeker, L. D., Whitlow, S. & Twickler, M. S. A 110,000-yr record of explosive volcanism from the GISP2 (Greenland) ice core. *Quat. Res.* **45**, 109–118 (1996).

37. Burke, A. et al. Stratospheric eruptions from tropical and extra-tropical volcanoes constrained using high-resolution sulfur isotopes in ice cores. *Earth Planet. Sci. Lett.* **521**, 113–119 (2019).

38. Baroni, M., Thiemens, M. H., Delmas, R. J. & Savarino, J. Mass-independent sulfur isotopic compositions in stratospheric volcanic eruptions. *Science* **315**, 84–87 (2007).

39. Baroni, M., Savarino, J., Cole-Dai, J., Rai, V. K. & Thiemens, M. H. Anomalous sulfur isotope compositions of volcanic sulfate over the last millennium in Antarctic ice cores. *J. Geophys. Res. Atmos.* **113**, D20 (2008).

40. Savarino, J., Romero, A., Cole-Dai, J., Bekki, S. & Thiemens, M. H. UV induced mass-independent sulfur isotope fractionation in stratospheric volcanic sulfate. *Geophys. Res. Lett.* **30**, 21 (2003).

41. Gautier, E. et al. 2600-years of stratospheric volcanism through sulfate isotopes. *Nat. Commun.* **10**, 1–7 (2019).

42. Cole-Dai, J. et al. Cold decade (AD 1810–1819) caused by Tambora (1815) and another (1809) stratospheric volcanic eruption. *Geophys. Res. Lett.* **36**, 22 (2009).

43. Wallace, J. M. & Hobbs, P. V. 1. Introduction and overview. in *Atmospheric science: an introductory survey*, 1–24 (Academic Press, 2006).

44. Burke, A. et al. High sensitivity of summer temperatures to stratospheric sulfur loading from volcanoes in the Northern Hemisphere. *Proc. Natl. Acad. Sci.* **120**, 47 (2023).

45. Lamarque, J. F. et al. Historical (1850–2000) gridded anthropogenic and biomass burning emissions of reactive gases and aerosols: methodology and application. *Atmos. Chem. Phys.* **10**, 7017–7039 (2010).

46. Gao, C., Robock, A. & Ammann, C. Volcanic forcing of climate over the past 1500 years: an improved ice core-based index for climate models. *J. Geophys. Res. Atmos.* **113**, D23 (2008).

47. Plummer, C. T. et al. An independently dated 2000-yr volcanic record from Law Dome, East Antarctica, including a new perspective on the dating of the 1450s CE eruption of Kuwae. *Vanuatu. Clim. Past.* **8**, 1929–1940 (2012).

48. Edmonds, M., Mason, E. & Hogg, O. Volcanic outgassing of volatile trace metals. *Annu. Rev. Earth Planet. Sci.* **50**, 79–98 (2022).

49. Ilyinskaya, E. et al. Rapid metal pollutant deposition from the volcanic plume of Kilauea, Hawai'i. *Commun. Earth Environ.* **2**, 1–15 (2021).

50. Sigurgeirsson, M. A. Hallmundarhraun. *Rannsóknargreinar* **92**, 5–16 (2022).

51. Sigl, M. et al. Insights from Antarctica on volcanic forcing during the Common Era. *Nat. Clim. Chang.* **4**, 693–697 (2014).

52. Haywood, J. & Boucher, O. Estimates of the direct and indirect radiative forcing due to tropospheric aerosols: a review. *Rev. Geophys.* **38**, 513–543 (2000).

53. Bellouin, N. et al. Bounding global aerosol radiative forcing of climate change. *Rev. Geophys.* **58**, 1 (2020).

54. Schmidt, A. et al. Importance of tropospheric volcanic aerosol for indirect radiative forcing of climate. *Atmos. Chem. Phys.* **12**, 7321–7339 (2012).

55. Carslaw, K. S. et al. Aerosols in the pre-industrial atmosphere. *Curr. Clim. Chang. Reports* **3**, 1–15 (2017).

56. Oman, L., Robock, A., Stenchikov, G. L. & Thordarson, T. High-latitude eruptions cast shadow over the African monsoon and the flow of the Nile. *Geophys. Res. Lett.* **33**, 18 (2006).

57. Zambri, B., Robock, A., Mills, M. J. & Schmidt, A. Modeling the 1783–1784 Laki Eruption in Iceland: 1. Aerosol evolution and global stratospheric circulation impacts. *J. Geophys. Res. Atmos.* **124**, 6750–6769 (2019).

58. Manning, J. G. et al. Volcanic suppression of Nile summer flooding triggers revolt and constrains interstate conflict in ancient Egypt. *Nat. Commun.* **8**, 900 (2017).

59. Iles, C. E., Hegerl, G. C., Schurer, A. P. & Zhang, X. The effect of volcanic eruptions on global precipitation. *J. Geophys. Res. Atmos.* **118**, 8770–8786 (2013).

60. Haywood, J., Jones, A., Bellouin, N. & Stephenson, D. Asymmetric forcing from stratospheric aerosols impacts Sahelian rainfall. *Nat. Clim. Chang.* **3**, 660–665 (2013).

61. Affolter, S. et al. Central Europe temperature constrained by speleothem fluid inclusion water isotopes over the past 14,000 years. *Sci. Adv.* **5**, 6 (2019).

62. Mangini, A., Spötl, C. & Verdes, P. Reconstruction of temperature in the Central Alps during the past 2000 yr from a  $\delta^{18}\text{O}$  stalagmite record. *Earth Planet. Sci. Lett.* **235**, 741–751 (2005).

63. Fohlmeister, J., Vollweiler, N., Spötl, C. & Mangini, A. COMNISPA II: update of a mid-European isotope climate record, 11 ka to present. *The Holocene* **23**, 749–754 (2013).

64. McCormick, M., Dutton, P. E. & Mayewski, P. A. Volcanoes and the climate forcing of Carolingian Europe, AD 750–950. *Speculum* **82**, 865–895 (2007).

65. Newfield, T. P. The contours, frequency and causation of subsistence crises in Carolingian Europe (750–950 CE). *InCrisis Alimentarias En La Edad Media: Modelos, Explicaciones Y Representaciones* **117**, 172 (2013).

66. Devroey, J.-P. *La Nature et le Roi. Environnement, pouvoir et société à l'âge de Charlemagne*, 740–820 (Albin Michel, 2019).

67. The Chronicle of Theophanes Confessor: Byzantine and Near Eastern History, AD 284–813, transl. with introduction and commentary by C. Mango, R. Scott, and G. Greatrex. (Clarendon Press, 1997).

68. Wozniak, T. *Naturereignisse im frühen Mittelalter. Das Zeugnis der Geschichtsschreibung vom 6. bis 11. Jahrhundert*. (De Gruyter, 2020).

69. Preiser-Kapeller, J. & Kislinger, E. The sun was darkened for seventeen days (AD 797). An interdisciplinary exploration of celestial phenomena between Byzantium, Charlemagne, and a volcanic eruption. *Mediev. Worlds* **17**, 3–58 (2022).

70. Kondrashov, D., Feliks, Y. & Ghil, M. Oscillatory modes of extended Nile River records (AD 622–1922). *Geophys. Res. Lett.* **32**, 10 (2005).

71. Iles, C. E. & Hegerl, G. C. Systematic change in global patterns of streamflow following volcanic eruptions. *Nat. Geosci.* **8**, 838–842 (2015).

72. Colose, C. M., LeGrande, A. N. & Vuille, M. Hemispherically asymmetric volcanic forcing of tropical hydroclimate during the last millennium. *Earth Syst. Dyn.* **7**, 681–696 (2016).

73. Booth, B. B., Dunstone, N. J., Halloran, P. R., Andrews, T. & Bellouin, N. Aerosols implicated as a prime driver of twentieth-century North Atlantic climate variability. *Nature* **484**, 228–232 (2012).

74. Chiang, J. C. & Friedman, A. R. Extratropical cooling, interhemispheric thermal gradients, and tropical climate change. *Annu. Rev. Earth Planet. Sci.* **40**, 383–412 (2012).

75. Hwang, Y. T., Frierson, D. M. & Kang, S. M. Anthropogenic sulfate aerosol and the southward shift of tropical precipitation in the late 20th century. *Geophys. Res. Lett.* **40**, 2845–2850 (2013).

76. Allen, R. J., Evan, A. T. & Booth, B. B. Interhemispheric aerosol radiative forcing and tropical precipitation shifts during the late twentieth century. *J. Clim.* **28**, 8219–8246 (2015).

77. Brönnimann, S. et al. Southward shift of the northern tropical belt from 1945 to 1980. *Nat. Geosci.* **8**, 969–974 (2015).

78. Schneider, L. et al. Revising midlatitude summer temperatures back to AD 600 based on a wood density network. *Geophys. Res. Lett.* **42**, 4556–4562 (2015).

79. Büntgen, U. et al. Prominent role of volcanism in Common Era climate variability and human history. *Dendrochronologia* **64**, <https://doi.org/10.1016/j.dendro.2020.125757> (2020).

80. Arosio, T. et al. Variable Response in Alpine Tree-Ring Stable Isotopes Following Volcanic Eruptions in the Tropics and Iceland. *Geosciences* **12**, 371 (2022).

81. Schneider, D. P., Ammann, C. M., Otto-Bliesner, B. L. & Kaufman, D. S. Climate response to large, high-latitude and low-latitude volcanic eruptions in the Community Climate System Model. *J. Geophys. Res. Atmos.* **114**, D15 (2009).

82. Zhong, Y. et al. Centennial-scale climate change from decadally-paced explosive volcanism: a coupled sea ice–ocean mechanism. *Clim. Dyn.* **37**, 2373–2387 (2011).

83. Van Dijk, E., Jungclaus, J., Lorenz, S., Timmreck, C. & Krüger, K. Was there a volcanic-induced long-lasting cooling over the Northern Hemisphere in the mid-6th–7th century? *Clim. Past* **18**, 1601–1623 (2022).

84. Maselli, O. J. et al. Sea ice and pollution-modulated changes in Greenland ice core methanesulfonate and bromine. *Clim. Past* **13**, 39–59 (2017).

85. Frei, K. M. et al. Was it for walrus? Viking Age settlement and medieval walrus ivory trade in Iceland and Greenland. *World Archaeol.* **47**, 439–466 (2015).

86. Young, N. E., Schweinsberg, A. D., Briner, J. P. & Schaefer, J. M. Glacier maxima in Baffin Bay during the Medieval Warm Period coeval with Norse settlement. *Sci. Adv.* **1**, 11 (2015).

87. Weiβbach, S. et al. Spatial and temporal oxygen isotope variability in northern Greenland—implications for a new climate record over the past millennium. *Clim. Past* **12**, 171–188 (2016).

88. Erhardt, T. et al. High-resolution aerosol data from the top 3.8 kyr of the East Greenland Ice coring Project (EGRIP) ice core. *Earth Syst. Sci. Data* **15**, 5079–5091 (2023).

89. Schrod, J. et al. Ice-nucleating particle concentrations of the past: Insights from a 600-year-old Greenland ice core. *Atmos. Chem. Phys.* **20**, 12459–12482 (2020).

90. Siggaard-Andersen, M. L., Steffensen, J. P. & Fischer, H. Lithium in Greenland ice cores measured by ion chromatography. *Ann. Glaciol.* **35**, 243–249 (2002).

91. Vinther, B. M. et al. A synchronized dating of three Greenland ice cores throughout the Holocene. *J. Geophys. Res.-Atmos.* **111**, D13 (2006).

92. Maselli, O. J., Fritzsche, D., Layman, L., McConnell, J. R. & Meyer, H. Comparison of water isotope-ratio determinations using two cavity ring-down instruments and classical mass spectrometry in continuous ice-core analysis. *Isotopes Environ. Health Stud.* **49**, 387–398 (2013).

93. Bowen, H. J. M. *Environmental Chemistry of the Elements*. (Academic Press, 1979).

94. Riley, J. P. & Tongudai, M. The major cation/chlorinity ratios in sea water. *Chem. Geol.* **2**, 263–269 (1967).

95. McLennan, S. M. Relationships between the trace element composition of sedimentary rocks and upper continental crust. *Geochem. Geophys. Geosyst.* **2**, 4 (2001).

96. Arienzo, M. M., McConnell, J. R., Chellman, N. & Kipfstuhl, S. Method for correcting continuous ice-core elemental measurements for under-recovery. *Environ. Sci. Technol.* **53**, 5887–5894 (2019).

97. Ruth, U., Wagenbach, D., Steffensen, J. P. & Bigler, M. Continuous record of microparticle concentration and size distribution in the central Greenland NGRIP ice core during the last glacial period. *J. Geophys. Res. Atmos.* **108**, 1–12 (2003).

98. Abbott, P. M. et al. Cryptotephra from the Icelandic Veiðivötn 1477 CE eruption in a Greenland ice core: confirming the dating of volcanic events in the 1450s CE and assessing the eruption’s climatic impact. *Clim. Past* **17**, 565–585 (2021).

99. Dunbar, N. W. et al. New Zealand supereruption provides time marker for the Last Glacial Maximum in Antarctica. *Sci. Rep.* **7**, 12238 (2017).

100. Jensen, B. J. L. et al. Transatlantic distribution of the Alaskan White River Ash. *Geology* **42**, 875–878 (2014).

101. McConnell, J. R. et al. Extreme climate after massive eruption of Alaska’s Okmok volcano in 43 BCE and effects on the late Roman Republic and Ptolemaic Kingdom. *Proc. Natl. Acad. Sci.* **117**, 15443–15449 (2020).

102. Smith, V. C. et al. The magnitude and impact of the 431 CE Tierra Blanca Joven eruption of Ilopango, El Salvador. *Proc. Natl. Acad. Sci.* **117**, 565–585 (2020).

103. Sun, C. et al. Ash from Changbaishan Millennium eruption recorded in Greenland ice: implications for determining the eruption’s timing and impact. *Geophys. Res. Lett.* **41**, 694–701 (2014).

104. Cook, E. et al. First identification of cryptotephra from the Kamchatka Peninsula in a Greenland ice core: Implications of a widespread marker deposit that links Greenland to the Pacific northwest. *Quat. Sci. Rev.* **181**, 200–206 (2018).

105. Büntgen, U. et al. Multi-proxy dating of Iceland’s major pre-settlement Katla eruption to 822–823 CE. *Geology* **45**, 783–786 (2017).

106. Mekhaldi, F. et al. Multiradionuclide evidence for the solar origin of the cosmic-ray events of 774/5 and 993/4. *Nat. Commun.* **6**, 1–8 (2015).

107. Sinnl, G. et al. A multi-ice-core, annual-layer-counted Greenland ice-core chronology for the last 3800 years: GICC21. *Clim. Past* **18**, 1125–1150 (2022).

108. Simonsen, M. F. et al. East Greenland ice core dust record reveals timing of Greenland ice sheet advance and retreat. *Nat. Commun.* **10**, 4494 (2019).

109. Hall, M. & Hayward, C. Preparation of micro- and crypto-tephras for quantitative microbeam analysis. *Geol. Soc. Spec. Publ.* **398**, 21–28 (2014).

110. Hartman, L. H. et al. Volcanic glass properties from 1459 CE volcanic event in South Pole ice core dismiss Kuwae caldera as a potential source. *Sci. Rep.* **9**, 14437 (2019).

111. Iverson, N. A., Kalteyer, D., Dunbar, N. W., Kurbatov, A. & Yates, M. Advancements and best practices for analysis and correlation of tephra and cryptotephra in ice. *Quat. Geochronol.* **40**, 45–55 (2017).

112. Kuehn, S. C. & Froese, D. G. Tephra from ice—a simple method to routinely mount, polish, and quantitatively analyze sparse fine particles. *Microsc. Microanal.* **16**, 218–225 (2010).

113. Pearce, N. J. G., Abbott, P. M. & Martin-Jones, C. Microbeam methods for the analysis of glass in fine-grained tephra deposits: a SMART perspective on current and future trends. *Geol. Soc. Spec. Publ.* **398**, 29–46 (2014).

114. Pearce, N. J. G., Denton, J. S., Perkins, W., Westgate, J. & Alloway, B. V. Correlation and characterisation of individual glass shards from tephra deposits using trace element laser ablation ICP-MS analyses: current status and future potential. *J. Quat. Sci.* **22**, 721–736 (2007).

115. Ranta, E. et al. Ancient and recycled sulfur sampled by the Iceland mantle plume. *Earth Planet. Sci. Lett.* **548**, 117452 (2022).

116. Jongbloed, U. et al. Underestimated passive volcanic sulfur degassing implies overestimated anthropogenic aerosol forcing. *Geophys. Res. Lett.* **50**; <https://doi.org/10.1029/2022GL102061> (2023).

117. Patris, N. et al. First sulfur isotope measurements in central Greenland ice cores along the preindustrial and industrial periods. *J. Geophys. Res. Atmos.* **107**, ACH 6-1 (2002).

118. Thode, H. Sulphur isotopes in nature and the environment: an overview. in *Stable Isotopes: Natural and Anthropogenic Sulphur in the Environment* (eds Krouse, H. & Grinenko, V. A.) 1–26 (Chichester: Wiley, 1991).

119. Sakai, H., Casadevall, T. J. & Moore, J. G. Chemistry and isotope ratios of sulfur in basalts and volcanic gases at Kilauea Volcano. *Hawaii. Geochim. Cosmochim. Acta* **46**, 729–738 (1982).

120. Mather, T. A. et al. Oxygen and sulfur isotopic composition of volcanic sulfate aerosol at the point of emission. *J. Geophys. Res. Atmos.* **111**, D18 (2006).

121. Martin, E., Bekki, S., Ninin, C. & Bindeman, I. Volcanic sulfate aerosol formation in the troposphere. *J. Geophys. Res. Atmos.* **119**, 12–660 (2014).

122. Farquhar, J., Bao, H. & Thiemens, M. Atmospheric influence of Earth's earliest sulfur cycle. *Science* **289**, 756–758 (2000).

123. Farquhar, J., Savarino, J., Airieau, S. & Thiemens, M. H. Observation of wavelength-sensitive mass-independent sulfur isotope effects during SO<sub>2</sub> photolysis: Implications for the early atmosphere. *J. Geophys. Res. E Planets* **106**, 32829–32839 (2001).

124. Farquhar, J. & Wing, B. A. Multiple sulfur isotopes and the evolution of the atmosphere. *Earth Planet. Sci. Lett.* **213**, 1–13 (2003).

125. Paris, G., Sessions, A. L., Subhas, A. V. & Adkins, J. F. MC-ICP-MS measurement of δ<sup>34</sup>S and Δ<sup>33</sup>S in small amounts of dissolved sulfate. *Chem. Geol.* **345**, 50–61 (2013).

126. Burke, A. et al. Sulfur isotopes in rivers: Insights into global weathering budgets, pyrite oxidation, and the modern sulfur cycle. *Earth Planet. Sci. Lett.* **496**, 168–177 (2018).

127. Gautier, E., Savarino, J., Erbland, J. & Farquhar, J. SO<sub>2</sub> oxidation kinetics leave a consistent isotopic imprint on volcanic ice core sulfate. *J. Geophys. Res. Atmos.* **123**, 9801–9812 (2018).

128. Traufetter, F., Oerter, H., Fischer, H., Weller, R. & Miller, H. Spatio-temporal variability in volcanic sulphate deposition over the past 2 kyr in snow pits and firn cores from Amundsenisen, Antarctica. *J. Glaciol.* **50**, 137–146 (2004).

129. Ferris, D. G., Cole-Dai, J., Reyes, A. R. & Budner, D. M. South Pole ice core record of explosive volcanic eruptions in the first and second millennia A.D. and evidence of a large eruption in the tropics around 535 A. D. *J. Geophys. Res. Atmos.* **116**, 1–11 (2011).

130. Luterbacher, J., Dietrich, D., Xoplaki, E., Grosjean, M. & Wanner, H. European seasonal and annual temperature variability, trends, and extremes since 1500. *Science* **303**, 1499–1503 (2004).

131. Osman, M. B., Coats, S., Das, S. B., McConnell, J. R. & Chellman, N. North Atlantic jet stream projections in the context of the past 1,250 years. *Proc. Natl. Acad. Sci.* **118**, e2104105118 (2021).

132. PAGES2k Consortium. A global multiproxy database for temperature reconstructions of the Common Era. *Sci. Data* **4**, 170088 (2017).

133. Dansgaard, W. Stable isotopes in precipitation. *Tellus* **16**, 436–468 (1964).

134. Hörhold, M. et al. Modern temperatures in central-north Greenland warmest in past millennium. *Nature* **613**, 503–507 (2023).

135. Siggaard-Andersen, M. NorthGRIP ice-core record of major ions measured using ion chromatography covering the last two millennia and additional short Holocene sections. PANGAEA, <https://doi.org/10.1594/PANGAEA.944172> (2022).

136. Plummer, C. T. NGRIP SO<sub>4</sub> data from the NGRIP 1996 main core and the NGRIP 2000 S6 shallow core. [https://www.iceandclimate.nbi.ku.dk/data/2012-12-03\\_NGRIP\\_SO4\\_5cm\\_Plummet\\_et\\_al\\_CP\\_2012.txt](https://www.iceandclimate.nbi.ku.dk/data/2012-12-03_NGRIP_SO4_5cm_Plummet_et_al_CP_2012.txt) (2012).

137. Sigl, M. & McConnell, J. R. NEEM-2011-S1 ice-core aerosol record (conductivity, NH<sub>4</sub>, NO<sub>3</sub>, BC, acidity, Na, Mg, S, Ca, Mn, Sr, Ce) in NW-Greenland at 2 cm resolution from 86–1997 CE on the annual-layer counted NS1-2011 chronology. PANGAEA, <https://doi.org/10.1594/PANGAEA.940553> (2022).

138. McConnell, J. R. NEEM\_2011\_S1 Ice Core. Arctic Data Center, <https://doi.org/10.18739/A2HX15R7T> (2013).

139. McConnell, J. Ice core aerosol measurements in the Tunu-N ice core. Arctic Data Center, <https://doi.org/10.18739/A2057CS7S> (2014).

140. McConnell, J. Tunu, Greenland 2013 Ice core chemistry. Arctic Data Center, <https://doi.org/10.18739/A2F18SF79> (2016).

141. McConnell, J. R. High-resolution elemental and chemical measurements in the NGRIP2 core, North Greenland. Arctic Data Center, <https://doi.org/10.18739/A20R9M558> (2023).

142. Mangini, A. et al. NOAA/WDS Paleoclimatology-Mangini et al. 2005 Spannagel Cave Stalagmite Oxygen Isotope Data and Temperature Reconstruction. NOAA, <https://doi.org/10.25921/7d43-qz5> (2005).

143. Toohey, M. & Sigl, M. Reconstructed volcanic stratospheric sulfur injections and aerosol optical depth, 500 BCE to 1900 CE, version 3, World Data Center for Climate (WDCC) at DKRZ. [https://doi.org/10.26050/WDCC/eVolv2k\\_v3](https://doi.org/10.26050/WDCC/eVolv2k_v3) (2019).

144. Hörhold, M., et al. Cation concentrations of the EGRIP ice core. PANGAEA, <https://doi.org/10.1594/PANGAEA.966039> (2024).

145. Hörhold, M., et al. Anion concentrations of the EGRIP ice core. PANGAEA, <https://doi.org/10.1594/PANGAEA.966041> (2024).

146. McConnell, J. & Chellman, N. Traditional and non-traditional volcanic fallout from 700 to 1300 CE measured in four Greenland ice cores. Arctic Data Center, <https://doi.org/10.18739/A2BK16R39> (2024).

147. Gabriel, I., et al. Geochemical composition of identified volcanic events from B19, TUNU2013, and RECAP Greenland ice cores and correlating proximal material. PANGAEA, <https://doi.org/10.1594/PANGAEA.967050> (2024).

148. Sigl, M., Gabriel, I., Hutchison, W. & Burke, A. Sulfate concentration and sulfur isotope data from Greenland TUNU2013 ice-core samples between 740–765 CE. PANGAEA, <https://doi.org/10.1594/PANGAEA.967047> (2024).

149. Sigl, M., McConnell, J. R. & Hörhold, M. Sulfur and volcanic sulfate deposition from 6 ice cores in Greenland. PANGAEA, <https://doi.org/10.1594/PANGAEA.967071> (2024).

150. Mackay, H. et al. The 852/3 CE Mount Churchill eruption: examining the potential climatic and societal impacts and the timing of the Medieval Climate Anomaly in the North Atlantic Region. *Clim. Past* **18**, 1475–1508 (2022).

151. Larsen, G. A brief overview of eruptions from ice-covered and ice-capped volcanic systems in Iceland during the past 11 centuries: Frequency, periodicity and implications. *Geol. Soc. Spec. Publ.* **202**, 81–90 (2002).

152. Moreland, W., Thordarson, T., Houghton, B. & Larsen, G. Driving mechanisms of subaerial and subglacial explosive episodes during the 10th century Eldgjá fissure eruption, southern Iceland. *Volcanica* **2**, 129–150 (2019).

153. Yang, Q. et al. The Millennium eruption of Changbaishan Tianchi volcano is VEI 6, not 7. *Bull. Volcanol.* **83**, 1–10 (2021).

154. Catalogue of Icelandic Volcanoes. <https://icelandicvolcanos.is/> (2014).

155. Hafnidalson, H., Eiriksson, J. & Van Kreveld, S. The tephrochronology of Iceland and the North Atlantic region during the middle and Late Quaternary: A review. *J. Quat. Sci.* **15**, 3–22 (2000).

156. Guðmundsdóttir, E. R., Larsen, G. & Eiríksson, J. Tephra stratigraphy on the North Icelandic shelf: extending tephrochronology into marine sediments off North Iceland. *Boreas* **41**, 719–734 (2012).

157. Óladóttir, B. A., Larsen, G. & Sigmarsdóttir, O. Volume estimates of nine Katla tephra layers. *Jökull* **64**, 23–40 (2014).

158. Óladóttir, B. A., Sigmarsdóttir, O., Larsen, G. & Thordarson, T. Katla volcano, Iceland: magma composition, dynamics and eruption

frequency as recorded by Holocene tephra layers. *Bull. Volcanol.* **70**, 475–493 (2008).

159. Bas, M. L., Maitre, R. L., Streckeisen, A., Zanettin, B. & Rocks, I. S. Chemical classification of volcanic rocks based on the total alkali-silica diagram. *J. Petrol.* **27**, 745–750 (1986).

160. Davies, S. M., Elmquist, M., Bergman, J., Wohlfarth, B. & Hammarlund, D. Cryptotephra sedimentation processes within two lacustrine sequences from west central Sweden. *The Holocene* **17**, 319–330 (2007).

161. Wastegård, S. & Davies, S. M. An overview of distal tephrochronology in northern Europe during the last 1000 years. *J. Quat. Sci. Publ. Quat. Res. Assoc.* **24**, 500–512 (2009).

162. Larsen, D. J., Miller, G. H., Geirsdóttir, Á. & Thordarson, T. A 3000-year varved record of glacier activity and climate change from the proglacial lake Hvítárvatn, Iceland. *Quat. Sci. Rev.* **30**, 2715–2731 (2011).

163. Davies, S. M., Turney, C. S. & Lowe, J. J. Identification and significance of a visible, basalt-rich Vedde Ash layer in a Late-glacial sequence on the Isle of Skye, Inner Hebrides. *Scotland. J. Quat. Sci. Publ. Quat. Res. Assoc.* **16**, 99–104 (2001).

164. Jennings, A. et al. Holocene tephra from Iceland and Alaska in SE Greenland shelf sediments. *Geol. Soc. London, Spec. Publ.* **398**, 157–193 (2014).

165. Lawson, I. T. et al. Environmental impacts of the Norse settlement: palaeoenvironmental data from Myvatnssveit, northern Iceland. *Boreas* **36**, 1–19 (2007).

166. Watson, E. J., Swindles, G. T., Lawson, I. T. & Savov, I. P. Do peatlands or lakes provide the most comprehensive distal tephra records? *Quat. Sci. Rev.* **139**, 110–128 (2016).

167. Streeter, R. & Dugmore, A. Late-Holocene land surface change in a coupled social-ecological system, southern Iceland: a cross-scale tephrochronology approach. *Quat. Sci. Rev.* **86**, 99–114 (2014).

168. Harning, D. J., Thordarson, T., Geirsdóttir, Á., Zalzal, K. & Miller, G. Provenance, stratigraphy and chronology of Holocene tephra from Vestfirðir, Iceland. *Quat. Geochronol.* **46**, 59–76 (2018).

169. Wastegård, S. Early to middle Holocene silicic tephra horizons from the Katla volcanic system, Iceland: New results from the Faroe Islands. *J. Quat. Sci.* **17**, 723–730 (2002).

170. Óladóttir, B. A., Sigmarsdóttir, O., Larsen, G. & Devidal, J. L. Provenance of basaltic tephra from vatnajökull subglacial volcanoes, Iceland, as determined by major- and trace-element analyses. *The Holocene* **21**, 1037–1048 (2011).

171. Larsen, G. & Eiríksson, J. Late Quaternary terrestrial tephrochronology of Iceland—frequency of explosive eruptions, type and volume of tephra deposits. *J. Quat. Sci. Publ. Quat. Res. Assoc.* **23**, 109–120 (2008).

172. Plunkett, G. & Pilcher, J. R. Defining the potential source region of volcanic ash in northwest Europe during the Mid- to Late Holocene. *Earth-Science Rev.* **179**, 20–37 (2018).

173. Meara, R. H. H., Thordarson, T. H., Pearce, N. J. G., Hayward, C. & Larsen, G. A catalogue of major and trace element data for Icelandic Holocene silicic tephra layers. *J. Quat. Sci.* **35**, 122–142 (2020).

132646 and CRSII2\_147674). This research benefited from the participation of the authors in the Volcanic Impacts on Climate and Society (VICS) working group of the Past Global Changes (PAGES) project. This work uses data from the NGRIP, EGRIP, and RECAP ice core projects directed and organised by the Physics of Ice, Climate and Earth, at the Niels Bohr Institute, Denmark. The authors acknowledge the scientific consortia and funding agencies associated with each ice core project. The collection and analysis of the TUNU2013 and NEEM-2011-S1 ice cores and partial support for this interpretation were funded by US National Science Foundation grants (no. 1204176, 909541, 1925417) to J.R.M. Continuous chemical analysis and interpretation of the NGRIP2 ice core at DRI was supported by the John Fell Oxford University Press Research Fund and All Souls College, Oxford. The B19 ice core was obtained as part of the North Greenland Traverse project, supported by the GRIP ice core drilling project. Analysis of the B19 ice core was funded by the Desert Research Institute, USA. M.S. and P.M.A. thank the Alfred Wegner Institute, Germany and the NSF-Ice core facility, USA for their hospitality and assistance when sampling the TUNU2013 and B19 ice cores. Thanks to Sepp Kipfstuhl for providing access to the B19 ice core. Thanks to Pierre Lanari, Coralie Vesin, and Hugo Dominguez Carranza for help with EPMA analysis at the University of Bern. Thanks to Kirstin Krüger for organising fieldwork in Iceland and Thor Thordarson for providing detailed information regarding the Hallmundarhraun lava field, support and guidance during fieldwork and sampling in Iceland. Thanks to Esther Gudmundsdóttir for providing Lake Lögurinn data for geochemical correlations. Thanks to Francis Ludlow for discussing documentary sources from Europe. We thank Evgenia Ilyinskaya and two anonymous reviewers for their insightful comments that helped improve the final version of the manuscript.

## Author contributions

I.G. and M.S. wrote the original manuscript and constructed figures. I.G., P.M.A., G.P., and E.C. undertook tephra major element geochemical analyses. I.G and J.T.S. undertook trace element geochemical analyses. M.S. and J.R.M. contributed ice-core glaciochemical records. J.R.M. contributed ice core samples for subsequent measurements of tephra, S isotope analysis. J.R.M. and N.C. drilled and undertook continuous measurements of ice cores with DRI. A.B., W.H., and P.S. analyzed S isotopes. D.F. contributed Milandre cave temperature reconstruction. M.H., M.B., and B.T. undertook sulfate, fluoride, and chloride analyses for the EGRIP ice core. B.A.O. contributed proximal information regarding Icelandic volcanic activity during the study time period. J.P.K. contributed historical documentary records. All authors contributed to improving and editing the paper.

## Competing interests

The authors declare no competing interests.

## Additional information

**Supplementary information** The online version contains supplementary material available at <https://doi.org/10.1038/s43247-024-01350-6>.

**Correspondence** and requests for materials should be addressed to Imogen Gabriel.

**Peer review information** *Communications Earth & Environment* thanks Evgenia Ilyinskaya and the other, anonymous, reviewer(s) for their contribution to the peer review of this work. Primary Handling Editors: Emma Nicholson and Aliénor Lavergne. A peer review file is available.

**Reprints and permissions information** is available at <http://www.nature.com/reprints>

**Publisher's note** Springer Nature remains neutral with regard to jurisdictional claims in published maps and institutional affiliations.

## Acknowledgements

I.G., P.M.A. and M.S. received funding from the European Research Council under the European Union's Horizon 2020 research and innovation programme (grant agreement no. 820047). M.S. received funding from the Geoscience Department and the NFR TOPPFORK project "VIKINGS" (grant no. 275191) at the University of Oslo. I.G. received funding from the Swiss Polar Institute and BNP Paribas Swiss Foundation. Tephra research by E.C. was funded by the ERC project 'ice2ice' (grant agreement 610055). W.H. and P.S. are funded by a UKRI Future Leaders Fellowship (MR/S033505/1). D.F. acknowledges funding from the Swiss National Science Foundation for funding research on speleothems from Switzerland (grant nos. CRSI22-

**Open Access** This article is licensed under a Creative Commons Attribution 4.0 International License, which permits use, sharing, adaptation, distribution and reproduction in any medium or format, as long as you give appropriate credit to the original author(s) and the source, provide a link to the Creative Commons licence, and indicate if changes were made. The images or other third party material in this article are included in the article's Creative Commons licence, unless indicated otherwise in a credit line to the material. If material is not included in the article's Creative Commons licence and your intended use is not permitted by statutory regulation or exceeds the permitted use, you will need to obtain permission directly from the copyright holder. To view a copy of this licence, visit <http://creativecommons.org/licenses/by/4.0/>.

© The Author(s) 2024